sciendo

Contributions to Geophysics and Geodesy Vol. 48/2, 2018 (113–132)

Radioactive characterization of Ar-Rassafeh Badyieh area (Area-2), Syria by using Statistical factor analysis technique

Jamal ASFAHANI,Rashad AL-HENT, Mosa AISSA

Atomic Energy Commission, P. O. Box 6091, Damascus, Syria
tel: +963116111926; fax: 963116112289, e-mail: cscientific@aec.org.sy (J. Asfahani)

Abstract: A scored lithological map including nine litho-factor units is established through applying the statistical factor analysis technique (SFAT) to aerial spectrometric data of Area-2 (Al-Rassafeh Area), which includes T.C, eU, eTh, K, eU/eTh, eU/K, and eTh/K. A model of four rotated factors F1, F2, F3, and F4 is adapted for representing 61712 data measured points in Area-2, where 90.3% of total data variance is interpreted. The isolated lithological units related to F1, F2, and F3 are characterized by an eU average of 2.15, 0.99, and 1.57 ppm respectively. Two geological scored pseudo-sections derived from the lithological scored map are established and analyzed in order to show the mutual environmental geological relationships between different lithological isolated units. This scored map will be the base for further geological investigations in Area-2. SFAT has proven its efficacy in the research study Area-2, and allowed the different isolated sectors to be characterized and interpreted geologically and radioactively.

Key words: Statistical factor analysis technique (SFAT), aerial spectrometry survey, stratigraphic, Al-Rassafeh area, Syria, environmental features

1. Introduction

Airborne gamma-ray spectrometric survey is one of the most important geo-exploration techniques oriented for uranium prospecting (*Hambleton-Jones et al., 1984*). This gamma spectrometric survey has been essentially oriented towards defining radioactive anomalies related to uranium mineralization. It can be also employed for investigating of other useful minerals and sometimes subsurface hydrocarbon accumulations (*Selley, 1998*). The gathered data of such a spectrometric radioactive gamma survey can be efficiently

doi: 10.2478/congeo-2018-0004

used for characterizing geological, structural and geochemical environment factors (*Aissa and Jubeli, 1997*), where it is possible to categorize the rock units in the study area, based on their radioactive responses.

The present paper concentrates on the application of the advanced statistical factor analysis technique (SFAT) on the aerial gamma spectrometric data of study area for clarifying more in details the radioactive geology and environmental features observed in the study area (Fig. 1).

A scored lithological map is established herein with its geological units, on which the radioactive anomalies observed in study area are identified.

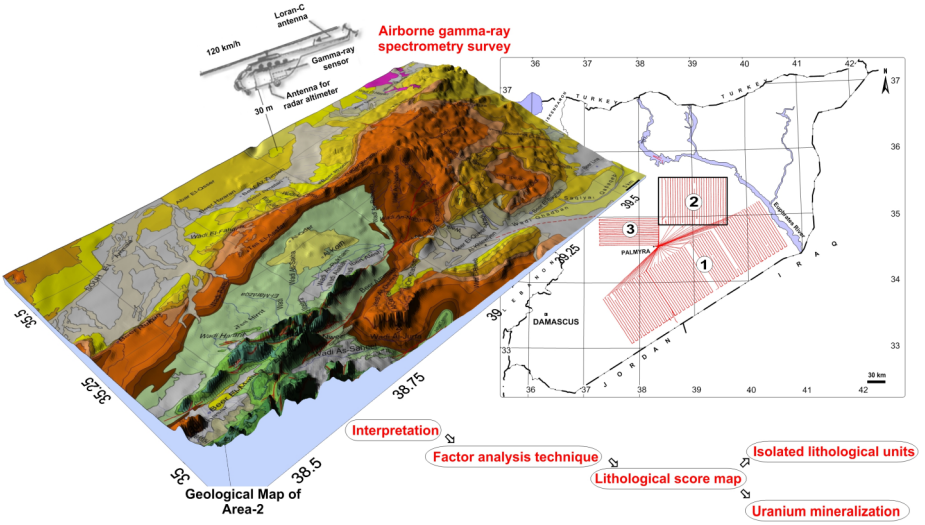

Fig. 1: Description of the study area and the investigation procedure scheme.

2. Object of study

The main objectives of this paper are therefore the following:

1. Asses the level of radioactivity TC, eU, eTh, and K, and determine the radioactive relationships with the geological and geochemical environments in the study region. The study region is particularly a very rugged terrain, where we ignore and have only a little information about its geology. A detailed field geological investigations are therefore extremely required. Such needed geological works are not actually an easy task to be carried

out in the near future, due to the present Syrian difficult conditions. The spectrometric gamma survey and its available data is therefore a powerful tool, and can be used for geologically characterizing the study region. Its application in the study replaces temporarily the field geological works, and remedies consequently the scarcity of geological information of the mentioned region.

2. Transfer the available geological map of the study into different isolated scored lithological units.
3. Analyze the mutual relationships between the different lithological isolated scored units at the light of available geology.
4. Interpreting the distinguished lithological scored units at the light of the available geology.

The first two objectives are achieved in the present research through the following:

1. Reinterpreting the aerial spectrometric gamma by applying SFAT.
2. Establishing the lithological scored map, with its different lithological units.

3. Area of study

The airborne gamma spectrometric technique was undertaken in Syria during a project conducted in 1987 in cooperation with the International Atomic Energy Commission and Riso National Laboratory SYR/86/005 (*Riso, 1987; Jubeli, 1990*).
This airborne survey was carried out in the following areas (Fig. 2A):

1. The Syrian Desert (Area-1) (7189 line km at 4 km line spacing).
2. Ar-Rassafeh Badyieh (Area-2) (2240 line km at 4 km line spacing).
3. The Northern Palmyrides (Area-3) (1600 line km at 3 km line spacing).

Fig. 2B shows the Syrian areas surveyed by airborne gamma-ray spectrometry, and the total radiometric map (T.C).

The present paper is concentrated on characterizing the radioactive behavior of Ar-Rassafeh Badyieh (Area-2) by using SFAT.

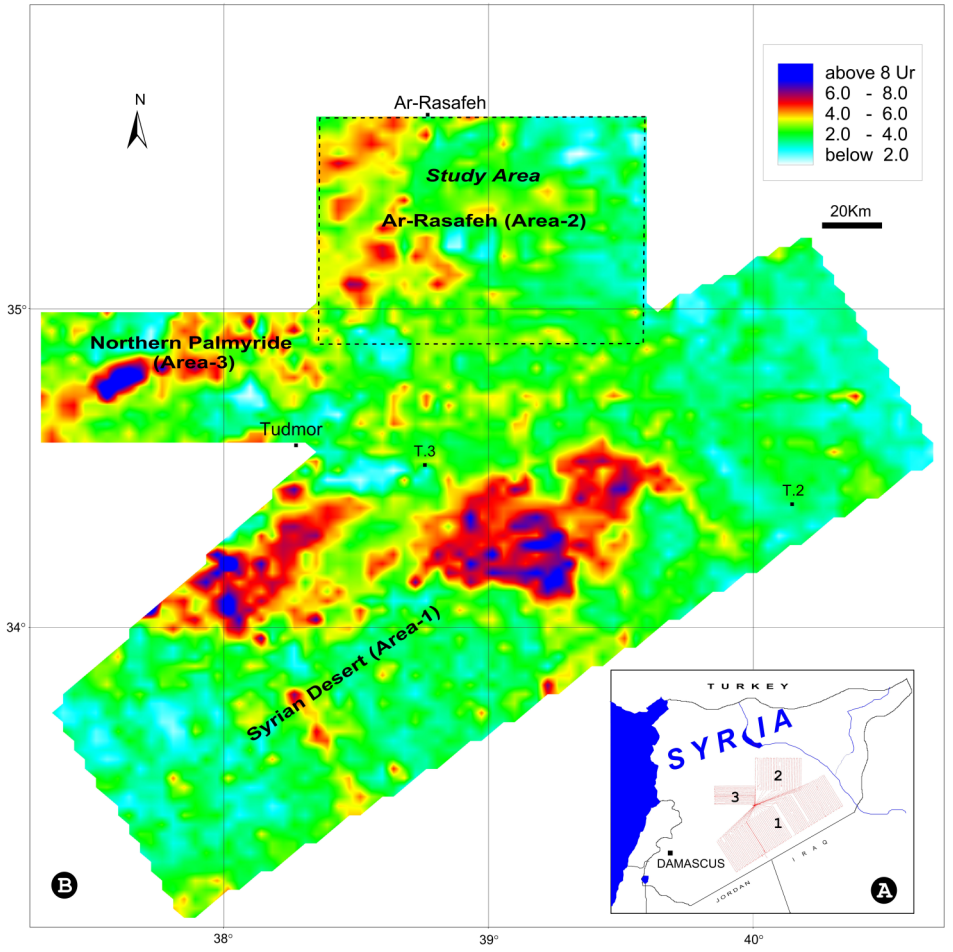

Fig. 2. (A) Total areas covered by airborne gamma-ray spectrometry in Syria. (B) Radiometric map resulting from spectrometric survey.

3.1. General Setting of the study area (Area-2)

Topography

The study area is considered as a transition zone between the low-mountain and the flat country. This mountain series form the northern limit of Palmyride range (Jabal AL-Bishri), the relief grades east, northeast and

southeastwards flood- plains, until it declines to Al-Furat river course in the north-east direction (out of the study area). The undulate sloping flood-plains are cut by many erosional valleys, where some of them are tectonogenetic (*Technoexport, 1966; JICA, 1996*).

Stratigraphy

Cretaceous, Paleogene litho-facies crop-out, while the Neogene and Quaternary sediments cover vast area of wadis and low-lands and flood- plain terraces of the studied territory, Fig. 3.

Cretaceous system: The Cretaceous litho- facies are mainly represented by carbonate, marly- clayey limestone, dolomitic limestone, ferruginous sandy limestone organic limestone, phosphate with remnants of fish bones, and flint concretions and bands, sometimes bituminous limestone intercalations, Fig. 3.

Paleogene system: the boundary between Cretaceous and Paleogene litho-facies is not prominent. Paleogene outcrops are zonally distributed in the studied territory. It is dominated by the carbonate litho-facies such as clayey limestone, sandy limestone with bitumen occurrences, dolomite, organic limestone, chalky-like limestone, marl, glauconitic- phosphate beds and flint, which are occurred in most of the cross-sections of the studied territory. Those facies denote the palio- shoreline and deltas within littoral zone, Fig. 3.

Neogene system: Cover vast tracts of the marginal plains adjacent of Al-Bishri anticline. The lithofacies of Neogene (*Technoexport, 1966; JICA, 1996*) denote a continental conditions start with sandy-clayey silt, conglomerates and sandstone with carbonate cement, breccia-like limestone, organic limestone, and dolomite with bitumen and gypsum alternations, Fig. 3.

Quaternary and recent system: Eluviation, eolian sands, pebbles of various genetic types and evaporates (*JICA, 1996*), Fig. 3.

Tectonic

The study area is located in the mobile part of Arabian platform slope in the northern marginal zone Palmyride folding system (*Dill, 2009; Technoexport, 1966*) (Fig. 3).

The study area is characterized as block folds, brachy-coffer anticlines, depressions, and regional deep faults. The Palmyride folding system is complicated by deep regional faults, which take north-eastern trend (*JICA, 1996;*

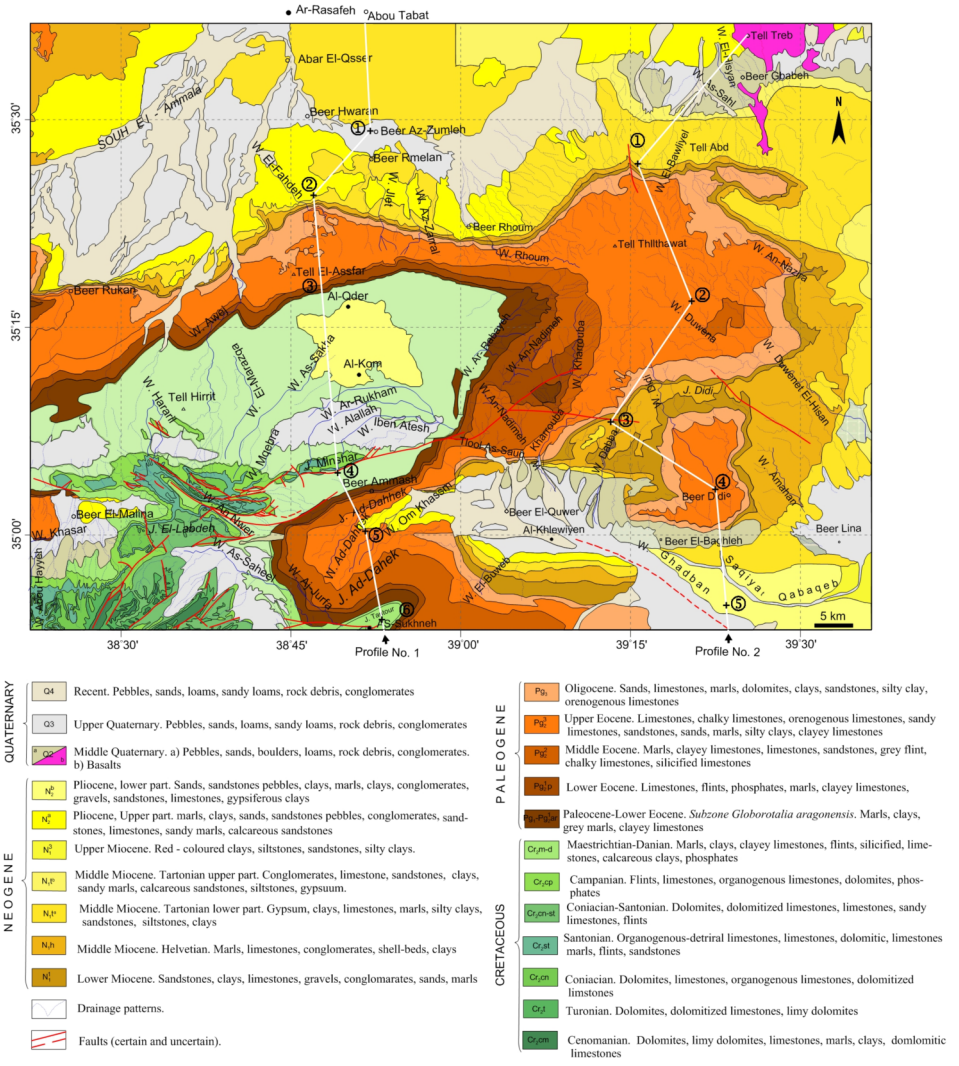

Fig. 3. Geological map of Ar-Rassafeh Badyieh (Area-2).

Litak et al., 1998). Faulted-flexures are also accompanied with coffer fold-axis. Most of those mentioned structural features are not marked at the surface, but inferred from geophysical data.

4. Methods of study

4.1. Aerial Gamma Spectrometric Technique

An airborne gamma-ray survey was carried out during 1987, over the Ar-Rassafeh Badyieh Area (Area-2) situated north of Syrian desert in the region between the northern Palmyrides in the south-west and the Euphrates in the northern and east. Area-2 were covered by 28 north-south oriented aerial survey lines. Those lines are of 80 km long, and spaced by 4 km, Fig. 2A. The typical survey speed was of 120 km/hr in a nominal survey, and the height was of 30 meters. A system of compact, lightweight, four-channel gamma-ray spectrometer, (GAD-6, Scintrex, Canada), with a detector of 12.5 litres NaI(Tl) volume has been used for conducting this aerial survey. The energy windows used in the four-channel gamma-ray spectrometer are shown in Table 1. The system calibration took place at the calibration pads at the Dala airport in Sweden (*Riso, 1987*). An IGI Loran-C navigation system was used to provide efficient flight path control. Potassium, uranium, thorium, and total gamma-ray counts were recorded over one-second intervals and stored on data tape together with the actual distance to the ground measured with a radar altimeter.

The raw data were corrected for background effects and the applicable interchange, Compton corrections. In addition, the exponential attenuation factors for height corrections were established (*Riso, 1987*).

Table 1. Range of energy with spectral windows used in airborne survey.

Window	Airborne Radiometric Survey (Mev)	Mainly Radioisotope
Potassium	1.38–1.56	K^{40}
Uranium	1.66–1.90	Bi^{214}
Thorium	2.44–2.77	Tl^{208}
Total-Count	0.40–2.77	–

4.2. Statistical Factor Analysis Technique (SFAT)

The aerial spectrometric data of the Ar-Rassafeh Badyieh (Area-2) have been subjected to a quantitative statistical factor analysis technique to establish lithological scored map for the study area with its various isolated lithological units. Using SFAT, a system of new factors is obtained through

transforming the origin data of seven radiometric variables measured in the study area (T.C, eU, eTh, K, eU/eTh, eU/K, and eTh/K). Those new factors are constrained to reproduce as much as possible the total variance of the origin data. Each original data point gains factor score, representing the affiliation of the samples to the newly defined factors. The plotting of these new factor produces a set of new maps. The new maps are qualitatively compared with the available geological map to extract the most important geological characteristics of the study area. This step serves as a tool in reinterpreting the data to provide direct differentiation of all the lithological units depending on the established lithological scored map and its reflection on the environmental aspects.

5. Results and discussion

Single and bivariate statistical analysis techniques are applied to the aerial gamma-ray spectrometric data related to Area-2, to characterize the seven radiometric variables as shown in Table 2. It was found that gamma-ray anomalies are mainly associated with phosphate deposits and encountered at adjoining parts of hydrocarbon fields in Syrian desert (*Jubeli et al., 1997*). The eU varies in Area-2 between a minimum of 0.16 ppm and a maximum of 13.61 ppm, with an average of 1.59 ppm and a standard deviation σ of 0.95 ppm. Higher values of uranium more than 3.50 ppm in the study area are considered as anomalous eU values, by adapting the threshold concept of $\overline{X} + 2\sigma$ (*Asfahani et al., 2009; Gavshin et al., 1974*).

Uranium also exhibits a relatively high value of coefficient of variability CV (59.75%), in comparing with those of eTh (33.9%) and K (34%). The high CV value for uranium is due to the higher mobility of the uranium as compared to eTh and K, which are characterized by higher stability under the same conditions, (*Asfahani, 2002; Asfahani et al., 2005; 2007; 2010*). The eTh varies in Area-2 between a minimum of 0.16 ppm and a maximum of 9.28 ppm, with an average of 3.39 ppm and a standard deviation σ of 1.15 ppm. The K varies in Area-2 between a minimum of 0.02 and a maximum of 0.85, with an average of 0.26 and a standard deviation σ of 0.09.

Table 3. shows the bivariate correlation analysis results and the correlation coefficients between the seven radiometric variables obtained while interpreting the data of Area-2.

Table 2. Statistical characteristics of the 7 radioactive variables in Area-2.

Variable	T.C	K (%)	eU (ppm)	eTh (ppm)	eU/eTh	eU/K	eTh/K
Case number	61712	61712	61712	61712	61712	61712	61712
Min	0.23	0.02	0.16	0.16	0.024	0.33	1.17
Max	17	0.85	13.61	9.28	25.79	446	185
$\overline{X}$	4.55	0.26	1.59	3.39	0.57	7.15	14.1
σ	1.36	0.09	0.95	1.15	0.57	7.11	6.28
CV	29.9	34	59.75	33.9	100	99	44.5
$\overline{X} + 2\sigma$	7.27	0.44	3.50	5.69	1.71	21.4	26.7

$\overline{X}$ – Mean, σ – Standard deviation,
CV – Coefficient of variability ($= \frac{\sigma}{\overline{X}} \cdot 100$).

Table 3. Correlation matrix of seven radiometric variables in Area-2.

Variables	**T.C**	**K**	**eU**	**eTh**	**eU/eTh**	**eU/K**	**eTh/K**
T.C	1						
K	0.61	1					
eU	0.68	0.04	1				
eTh	0.45	0.56	–0.16	1			
eU/eTh	0.27	–0.22	0.74	–0.52	1		
eU/K	0.21	–0.41	0.67	–0.34	0.68	1	
eTh/K	–0.2	–0.49	–0.16	0.29	–0.24	0.26	1

This correlation matrix shows a cluster of positive correlation between T.C and K (0.61), eU (0.68) and eTh (0.45). Positive correlation has also been found between K and eTh (0.56).

The above matrix is used to obtain seven un-rotated loading factors, which are difficult to be interpreted in geological terms. It is therefore necessary to rotate these seven factors to another form equivalent to the original un-rotated matrix. This rotation is achieved by using the varimax method to maximize the discriminability of the factors (*Comery, 1973*). The system of seven un-rotated factors are consequently reduced to only four principals factors F1, F2, F3 and F4 without losing significant information. In other words, varimax method allows a reduction from the original data system of seven dimensional factors into four interpretable principal factors (F1, F2, F3 and F4).

The results of this rotation are shown in Table 4. The four rotated factors are quite interpretable and represent 90.26% of the total system information, which is sufficient to interpret the variable data of Area-2 as shown in

Table 4. Eigen value of four rotated factors in Area-2.

	Eigen value	Total variance, %	Cumulative eigen value	Cumulative, %
F1	2.43	34.74	2.43	34.74
F2	1.93	27.57	4.36	62.31
F3	1.83	26.12	6.19	88.44
F4	0.128	1.83	6.32	90.26

Table 5.

The factor score coefficients shown in Table 6 are used to construct the three standard factor scored maps for F1, F2 and F3, for Area-2 as shown in Figs. 4, 5 and 6. F4 was not constructed because of its small eigen value of 0.128 from one side, and no clear geological significance is evident to be related with this factor from other side.

F1 explains 34.74% of the total variance, and has high loading values of 0.93, 0.82, and 0.85 for the variables of eU, eU/eTh, and eU/K respectively. This factor is therefore composed of those three variables and directly related to the uranium presence in the phosphorite of Cretaceous and Paleogene ages, outcropped in Area-2, Fig. 3 and Fig. 4, (*Slansky, 1986; Dill,*

Table 5. The four rotated factors in Area-2.

Variables	F1	F2	F3	F4
T.C	0.5	–0.13	0.798	0.15
K	–0.16	–0.48	0.799	–0.07
eU	0.93	–0.087	0.2	0.2
eTh	–0.33	0.31	0.82	0.029
eU/eTh	0.82	–0.2	–0.22	0.0005
eU/K	0.85	0.31	–0.17	–0.27
eTh/K	–0.064	0.98	–0.04	–0.03

Table 6. Factor score coefficients for Area-2.

Variables	F1	F2	F3	F4
T.C	0.155	0.036	0.46	0.213
K	–0.058	–0.128	0.387	–0.62
eU	0.46	0.04	–0.015	1.028
eTh	–0.099	0.124	0.34	–0.09
eU/eTh	0.103	–0.034	–0.06	–0.02
eU/K	0.39	0.059	0.02	–1.34
eTh/K	–0.036	0.87	0.12	0.25

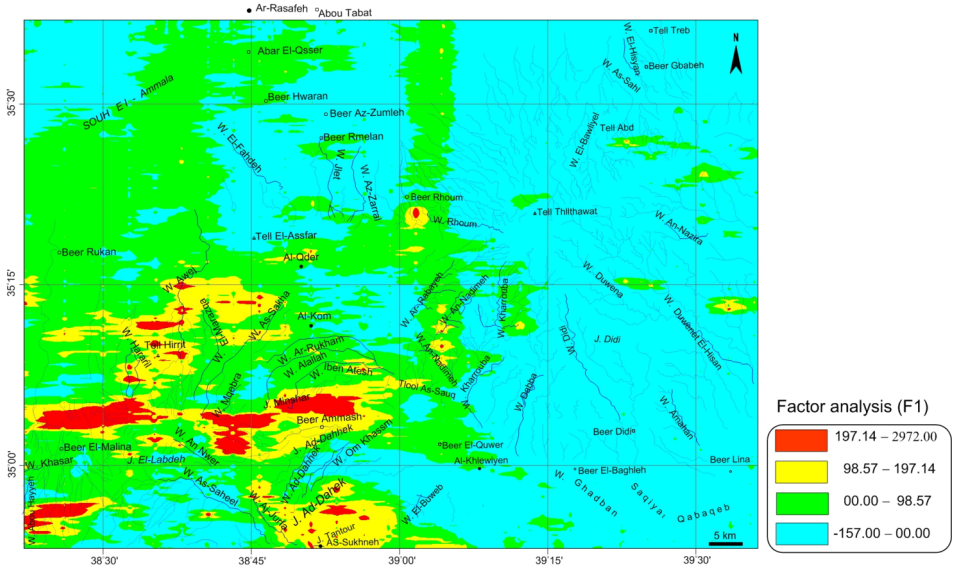

Fig. 4. Score map of F1 in Ar-Rassafeh Badyieh (Area-2).

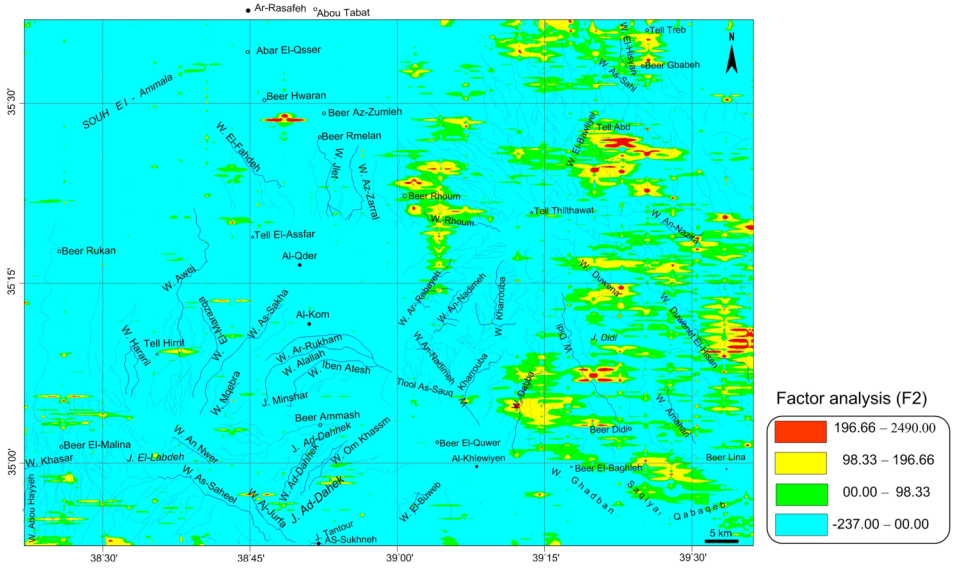

Fig. 5. Score map of F2 in Ar-Rassafeh Badyieh (Area-2).

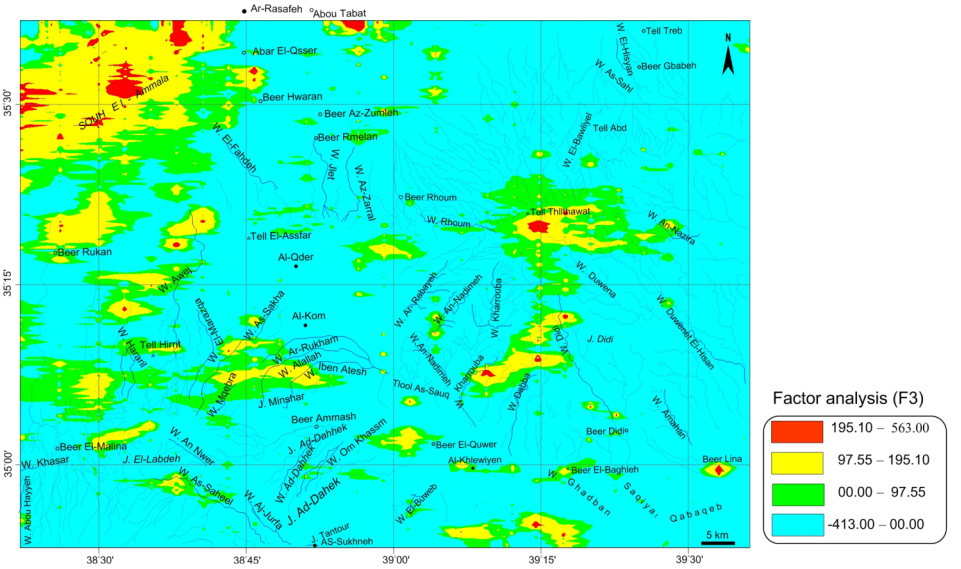

Fig. 6. Score map of F3 in Ar-Rassafeh Badyieh (Area-2).

2009). It is therefore called as *phosphate-uranium factor*.

The secondary uranium mineralizations are mostly concentrated along the marginal-faulted zones of the brachi-form anticline at the adjoined outcropped limits between late Cretaceous and lower Paleogene phosphatic and silicious rocks. The F1 factor shows a significant relationship between phosphate lithofacies and secondary uranium mineralizations, where the upward leaching and erosional loads drop along the marginal parts of active tectonic zones (*Wescott and Ethridge, 1980; Iilende, 2012*).

F2 explains 27.57% of the variability of geophysical data. It is negatively loaded for the K variable (–0.48), and positively for eTh/K (0.98). It is related to the facies, which are mostly composed of surficial washing and abrading products, characterized by prevailing of clayey facies, as marly clay, organic limestone, sandy limestone, sandy clay, sandy varieties intercalated with clayey limestone, silty clay, phosphorite and glauconite sands belonging to the Lower and Middle Paleogene, Fig. 3 and Fig. 5, (*Technoexport, 1966*). It is called as *littoral paleo-delta and alluvium fans factor*.

F3 explains 26.12% of the data variability, and is highly loaded with K (0.799) and eTh (0.82). This factor is related to the flood-closed basins,

evaporation pans, bitumen appearances, and paleo-channels of tectonic origin, Fig. 3 and Fig. 6, (*Heath et al., 1984; Dickson, 1984; Al-Kawaz and Aljubouri, 2006*). F3 is called as *closed seasonal basin factor.*

F4 explains only 1.83% of the data variability, and is difficult at this stage for F4 to be geologically interpreted.

Table 7 shows that F1 is the highest in eU in comparing with F2 and F3. The eU in the area dominated by F1 varies between 0.16 and 13.6 ppm with an average of 2.15 ppm. The area dominated by F2 and F3 are characterized by comparable values of eTh and K, which are higher than those related to area dominated by F1. The eTh in the area dominated by F2 varies between 0.24 and 8.57 ppm with an average of 3.35 ppm. The K in the area dominated by F2 varies between 0.02 and 0.75 with an average of 0.24. The eTh in the area dominated by F3 varies between 0.16 and 9.28 ppm with an average of 3.70 ppm. The K in the area dominated by F3 varies between 0.04 and 0.85 with an average of 0.30.

Table 7. Statistical characteristics of the 4 radioactive variables for F1, F2 and F3 in Area-2.

	F1				F2				F3			
Variables	Min.	Max.	Mean	σ	Min.	Max.	Mean	σ	Min.	Max.	Mean	σ
T.C	0.23	17.11	4.93	1.43	0.56	7.38	3.67	0.88	0.54	12.02	4.86	1.31
K	0.02	0.63	0.24	0.08	0.02	0.75	0.24	0.07	0.04	0.85	0.30	0.10
eU	0.16	13.61	2.15	1.17	0.16	4.04	0.99	0.51	0.16	4.58	1.57	0.68
eTh	0.17	6.94	2.80	1.01	0.24	8.57	3.35	0.97	0.16	9.28	3.70	1.18

A scored lithological map is constructed through the comparison and matching between the established scored maps of F1, F2 and F3 (Figs. 4, 5 and 6) and the available geological map of the study area (Area-2) (Fig. 3) as shown in Fig. 7.

The established lithological scored map includes nine litho-factor units, described as presented in Table 8. Table 8 shows the ranges of the standard factor scores (F1, F2 and F3), that characterize the geological units of Area-2, and the litho-factor description of those units.

Geological field observations gathered during surfacial radiometric surveys project and lithological comparative columnar sections of (*Technoexport, 1966*) are used as a support to study two selected profiles (Profile No. 1 and Profile No. 2) located and shown in Figs. 3 and 7.

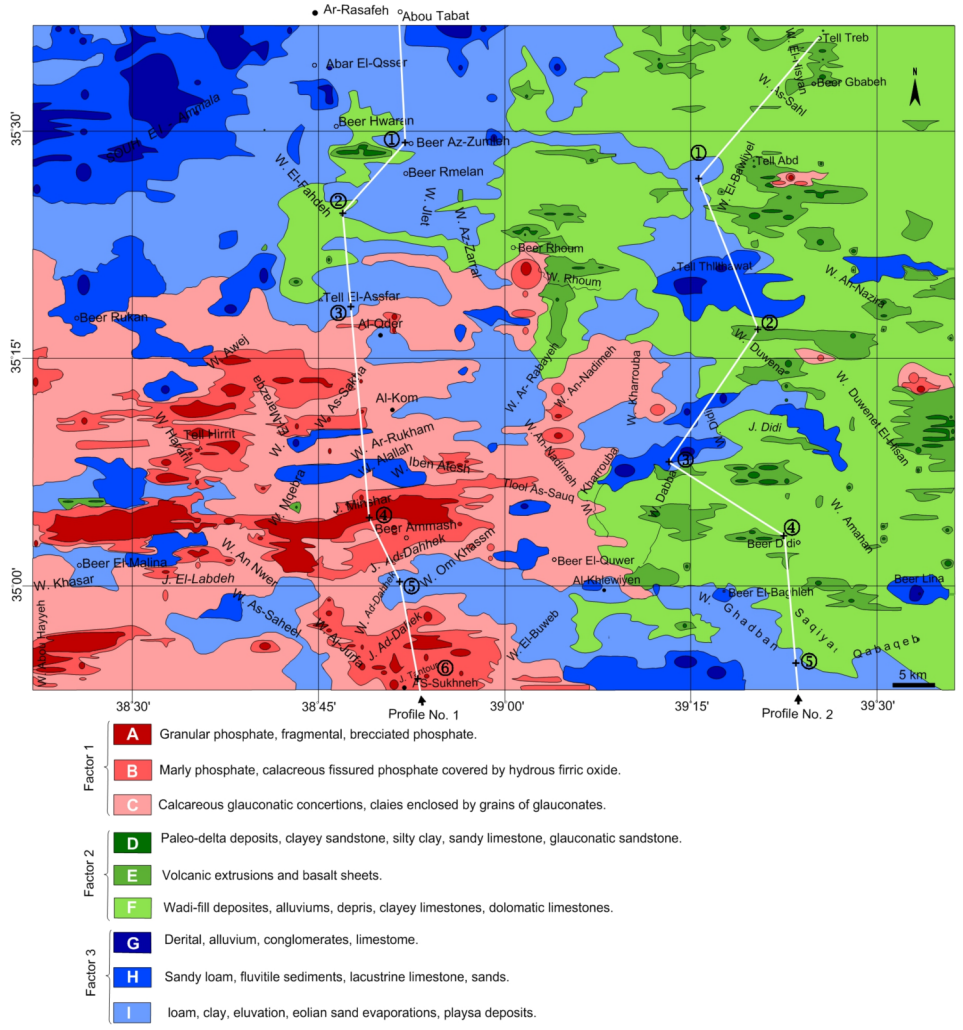

Fig. 7. Radiometric lithological scored map of Ar-Rassafeh Badyieh (Area-2).

The study of those two profiles is to delineate the phosphate sequences and to define favorable litho-facies for secondary uranium accumulation, and to delineate the subsurface structures. Those structures could be as significant structural and litho-stratigraphic traps, that must be localized for more geological details, Figs. 8 and 9.

Mutual geological relationships between the above distinguished nine lithological units (Table 8) along those two Profile No. 1 and Profile No. 2 have been analyzed, interpreted and discussed.

Profile No. 1: traverses through the core of brachi-form anticline of Cretaceous rocks, and passes through the faulted zone of the northern and southern flank of the anticline, Fig. 3. The pseudo-section drown along Profile No. 1 represents mostly the litho-factor units of F1, which reflect the secondary uranium mineralizations in phosphate beds of Upper Cretaceous rocks, Fig. 8. The other two factors F2 and F3 occupy the rest of the northern flank of the brachi-anticline and the adjacent plains related to Paleogene, Neogene and Quaternary, Fig. 8. The F2 and F3 litho-facies are characterized by prevalence of shallow marine environment and grade into lagoonal facies to paleo-delta and shore-line.

Profile No. 2: traverses through the eastern plunged flank of uplift (Al-Bishri), Fig. 3. The litho-facies along Profile No. 2 pass gradually from the

Table 8. Standard factor scores of the nine litho-factor units in Area-2.

Factor	Rock units	litho-factor range		Litho-facies description	Notices
F1	A	> 197.14		Granular phosphate, fragmental, brecciated-phosphate.	F1 is called as phosphate-uranium factor.
	B	98.57	197.14	Marly phosphate, calcareous- fissured phosphate covered by hydrous ferric oxide.	
	C	< 98.57		Calcareous glauconatic concretions, calcite- grains enclosed by glauconite.	
F2	D	> 196.66		Paleo-delta deposits, clayey sandstone, silty clay, sandy limestone, glauconatic sandstone.	F2 is called as littoral, paleo-delta and alluvium fans factor.
	E	98.33	196.66	Volcanic extrusions and basalt sheets.	
	F	< 98.33		Valley- fill deposits, alluviums, debris, clayey limestone, dolomatic limestone.	
F3	G	> 195.10		Detrital, alluvium, conglomerates, limestone.	F3 is called as closed seasonal basin factor.
	H	97.55	195.10	Sandy loam, fluvial sediments, lacustrine limestone, sands.	
	I	< 97.55		loam, clay, eluviation, eolian sand evaporates, and playa deposits.	

littoral zone to continental environments to turn finally into semi-closed seasonal basins, Fig. 9. The established scored pseudo-section of Profile No. 2 mainly shows the litho-facies related to F2 and F3, with the clayey-silty lacustrain carbonate and evaporates domination.

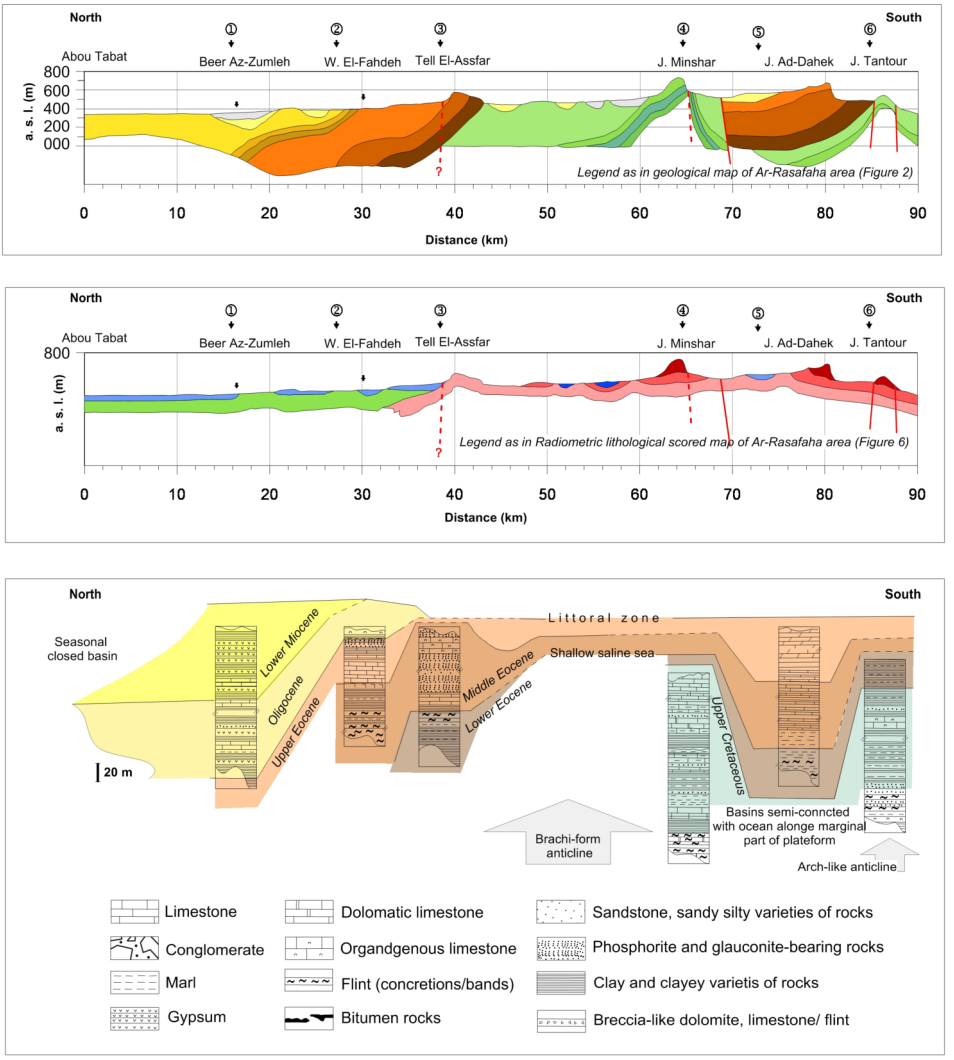

Fig. 8. Pseudo-section profile. No. 1 passing by different distinguished litho-factor units.

The faults indicated in Figs. 8 and 9 play in addition to litho-facial structure an important role in increasing radioactivity. Their evident role is shown in SW direction of profile No. 1, where high radioactivity is noticed. In fact, such an observed radioactivity is due to the uranium mobilization caused by ascending of solutions flows through those faults. In the other side, the role of the faults indicated in the other parts of the study area particularly in NE direction (Fig. 9) is limited because of two reasons; firstly

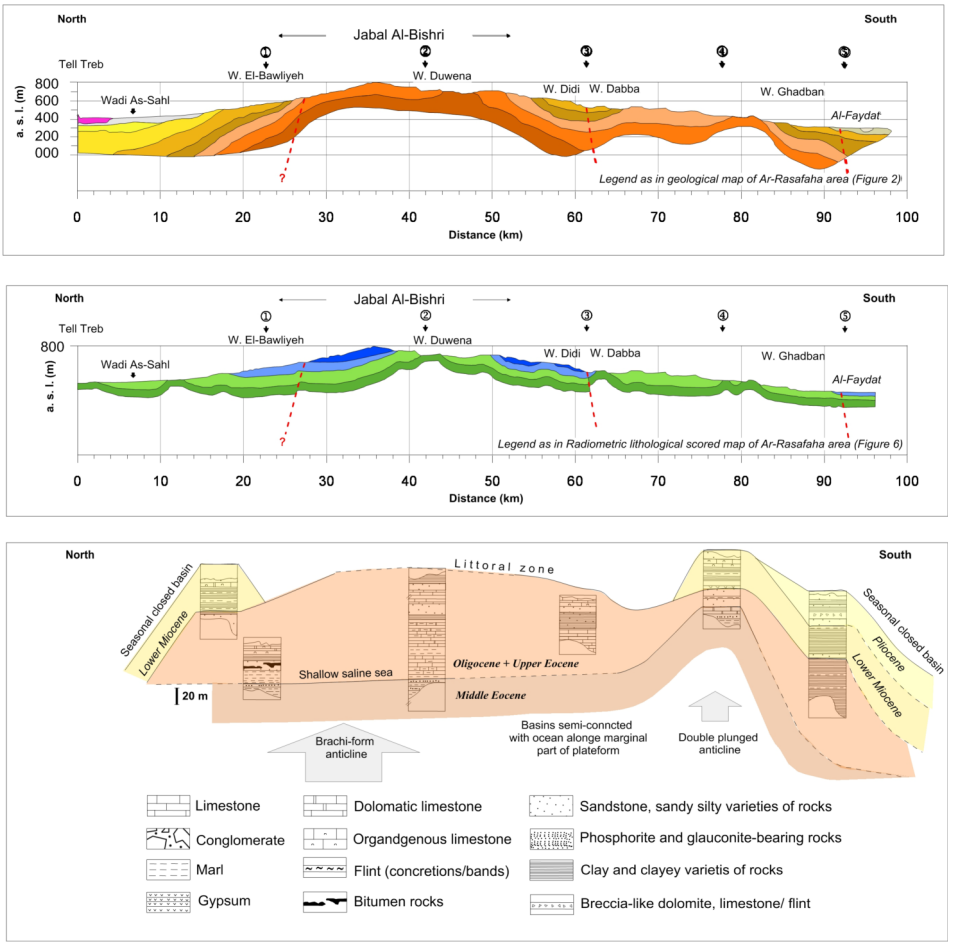

Fig. 9. Pseudo-section profile. No. 2 passing by different distinguished litho-factor units.

those faults may be buried under sediments cover of Neogene deposits, and secondly the superficial leaching is more prevailed than the deep- ascendant solution leaching.

The study and analysis of those two profiles give important geological insights on the geology of the study area. Those insights will be efficacy exploited when detailed field geological and geochemical mining investigations will be carried out.

6. Conclusions

Statistical factor analysis technique (SFAT) is applied in this research for interpreting aerial spectrometric data of Area-2 in Syria. The different obtained results in this paper are mainly oriented toward understanding the mutual relationships between different lithological units localized in a complicated geological area. The areas dominated by the resulting rotated three factors F1, F2, and F3 have been radioactively characterized for the parameters of T.C, eU, eTh, and K. Lithological scored map containing nine litho-factor units has been established through applying SFAT. The characteristics of those litho-factor units have been described through interpreting the established radioactive factors maps of F1, F2, and F3. Those defined litho-factor units will be the base for further geological and environmental investigation in Area-2. Two geological scored pseudo-section profiles (Profile No. 1 and Profile No. 2) have been selected and analyzed to show the mutual geological- environmental relationships between the different isolated lithofacies. SFAT has demonstrated its capability in dividing the study area to different isolated environments, where each one is characterized by its specific geology and radioactivity. The SFAT enables geophysicists to quickly establish radiometric maps with a least amount of subjectivity. This advanced statistical technique is therefore recommended to be applicable in dealing with other huge aerial spectrometric data related to other regions. SFAT tool has a strong potential in both geological and environmental mapping and locating areas of radioactive anomalies. The acquired knowledge of this paper will be potentially employed later, when detailed geological and geochemical mining investigations are lanced for radiometric and other useful elements prospecting.

Acknowledgements. Dr. I. Othman, General Director of Syrian Atomic Energy Commission is thanked for his permission to publish this paper. The anonymous reviewers are deeply thanked for their professional remarks and critics. Their suggestions improved significantly the final version of this paper. Dr. Igor Kohut, the editor of Contribution to Geophysics and Geodesy is thanked for his collaboration and editing of this paper.

References

Aissa M., Jubeli Y., 1997: Carborne gamma-ray spectrometric survey of an Area, East of Homs, central Syria. Applied Radiation and Isotopes, **48**, 1, 135–142.

Al-Kawaz H. A., Aljubouri Z. A., 2006: Mineralogy and petrography of marl sediments within the Fat'ha formation in selected parts of northern Iraq. Raf. Jour. Sci., **17**, 1, 19–31.

Asfahani J., 2002: Phosphate prospecting using natural gamma ray well logging in the Khneifiss Mine, Syria. Exploration and Mining Geology, **11**, 61–68.

Asfahani J., Aissa M., Al-Hent R., 2005: Statistical factor analysis of aerial spectrometric data, Al-Awabed area, Syria: a useful guide for phosphate and uranium exploration. Appl. Rad. Isot., **62**, 649–661.

Asfahani J., Aissa M., Al-Hent R., 2007: Uranium Migration in Sedimentological Phosphatic Environment in Northern Palmyrides, Al-Awabed Area, Syria. Appl. Rad. Isot., **65**, 1078–1086.

Asfahani J., Al-Hent R., Aissa M., 2009: Uranium statistical and geological evaluation of airborne spectrometric data in the Al-Awabed region and its surroundings (Area-3), Northern Palmyrides, Syria. Appl. Rad. Isot., **67**, 654–663.

Asfahani J., Aissa M., Al-Hent R., 2010: Aerial Spectrometric Survey for Localization of Favorable Structures for Uranium Occurrences in Al-Awabed Area and its Surrounding (Area-3), Northern Palmyrides, Syria. Appl. Rad. Isot., **68**, 219–228.

Comery A. L., 1973: A first course in factor analysis. Academic Press, New York, 316p.

Dill H. G., 2009: A comparative study of uranium-thorium accumulation at the western edge of the Arabian Peninsula and mineral deposits worldwide. Arabian Journal of Geosciences, **4**, 12, 123–146, doi: 10.1007/s12517-009-0107-4.

Dickson B. L., 1984: Uranium series disequilibrium in the carnotite deposits of western Australia. Technical document issued by the IAEA, Vienna, IAEA-Tecdoc-322.

Gavshin V. M., Bobrov V. A., Zorkina L. S., 1974: Quantitative relation between uranium and phosphorus in phosphorite and phosphatic sedimentary rocks. Litho. Min. Deposit, **6**, 118–126 (English transl. 740–746).

Hambleton-Jones B. B., Heard R. G., Tdens P. D., 1984: Exploration for surficial uranium deposits. Surficial uranium deposits, TECDOC, 322, IAEA, Vienna, 1984.

Heath A. G., Deutscher R. L., Butt R. M., 1984: Lake Austin uranium deposit western Australia. Technical document issued by the IAEA, Vienna, IAEA-Tecdoc-322.

Iilende A., 2012: The surface of uranium and vanadium at the Langer Heinrich and Klein Trekkopje uranium deposits-genesis and controlling factors for uranium mineralization. University of Namibia, Thesis 9507566.

Japan International Cooperation Agency (JICA), 1996: The study on water resources development the northwestern and central basins in the Syrian Arab Republic (Phase I), progress report, December 1996. NIPPON KOEI Co., LTD. SANYU CONSULTANTS INC. Tokyo, Japan.

Jubeli Y. M., 1990: Uranium exploration in Syria SY/86/005, Final report. Atomic Energy Commission of Syria, Damascus.

Jubeli Y. M., Aissa M., AL-Hent R., 1997: Merging airborne and carborne radiometric data for survey DEIR-AZ-ZOR area, Syria, Applied Radiation and Isotope, **48**, 5, 667–675.

Litak R. K., Barazangi M., Brew G., Sanaf T., Al-Emam A., 1998: Structure and evolution of the petrol ferrous Euphrates graben system, south east Syria. Aapg belle ton, **82**, 6, 1173–1190.

Riso, 1987: Aerial gamma-ray in Syria YR/87/005. Technical report. Riso National Laboratory, Roskilde, Denmark.

Selley R. C., 1998: Elements of petroleum geology (Second edition). Chapter 3: Methods of exploration. Academic Press, 490 p.

Slansky M., 1986: Geology of sedimentary phosphates. Book, Elsevier science publishing co., INC, 52 Vanderbilt Avenue, New York 10017.

Technoexport, 1966: Explanatory notes on the geological map of Syria, mineral deposits and underground-water resources. Ministry of Geology, USSR, 1967.

Wescott W. A., Ethridge F. G., 1980: Fan-delta sedimentology and tectonic setting – Yallahs fan delta, Southeast Jamaica. American Association of Petroleum Geologists Bulletin, **64**, 3, 374–399.

sciendo

Contributions to Geophysics and Geodesy Vol. 48/2, 2018 (133–160)

An optimal multiscale approach to interpret gravity data using successive decomposition of the Bouguer anomaly

Mohamed ARFAOUI[1,2], Mohamed Hedi INOUBLI[2], Adnen AMIRI[2]

[1] Office National des Mines,
24, Rue de l'Energie, 2035, La Charguia, Tunis, Tunisia; e-mail: mohamarfaoui@gmail.com

[2] Unité de Recherche de Géophysique Appliquée aux Matériaux et aux Minerais, Université Tunis-El Manar, Faculté des Sciences de Tunis, 2092 El Manar, Tunis, Tunisia

Abstract: A multiscale interpretive approach is presented to identify multiscale discontinuities and sources boundaries, and to obtain comprehensive pseudo-section density images of 2D structures at depth. This interpretive approach is based on the total horizontal gradient and apparent density operator applied to the gravity anomalies of pseudo-depth slices derived from the successive decomposition of the Bouguer anomaly. This approach is applied to gravity data from the northwestern part of Tunisia, it provides the fault system repartition at different depths and describes the density distribution within the basins and trough. Thus, the NW–SE and NE–SW faults are the deepest whereas the N–S and E–W faults are relatively superficial. The density pseudo-sections reveal the vertical continuity of salt Triassic outcrops of Jebel Debadib as well as a diapiric model, the presence of a Triassic salt dome in the Kalaa El Khasba through and dense series under the Miopliocene and Quaternary deposits of the Mejarda basin.

Key words: Gravity anomalies, Tunisia, Multiscale discontinuities, Pseudo-depth slices, Pseudo-section density

1. Introduction

Gravity surveys are designed to delineate geologic structures at depth by interpretation of observed data. The essential question is to find a quantitative and qualitative interpretive process for determining 3D locality and density of causative sources. Generally interpretation of gravity data follows three principle strategies: (1) anomaly separation, (2) identifying source boundaries and discontinuities, and (3) resolving sources at depth, which includes depth determination and source density.

doi: 10.2478/congeo-2018-0005

Anomaly separation into regional and residual components by decomposition is commonly used in gravity interpretation. Short wavelength components associated with near surface geologic bodies are separated from long wavelength features associated with deep seated structures. Decomposition may be achieved by least squares fitting of polynomial surfaces (*Simpson, 1954*), wavenumber filters as an upward continuation (*Gupta and Ramani, 1980*), Gaussian function (*Arfaoui et al., 2015*), or bandpass Wiener optimum filters (*Pawlowsky and Hansen, 1990*). Since the Bouguer anomaly is the sum of several components caused by deep seated, intermediate and near surface geologic bodies the gravity effect of those sources may be estimated from a successive decomposition process where the decomposition "bootstraps" to greater depths with each iteration (*Arfaoui et al., 2011*).

Sources boundaries and discontinuities are usually defined by several different derivative operators. These discontinuities generally correspond with high density contrast zones associated with geological contacts and faults. Various derivative operators have been developed for enhancing the gravity signal. They are designed using a combination of simple gravity gradients and have been tested by many studies. One fundamental study was realized by *Cordell and Grauch (1982, 1985).* They used the maximum total horizontal gradient to map boundaries between domains of uniform density and magnetic susceptibility. The use of this operator was improved and automated (*Blakely and Simpson, 1986*) by assigning a quality factor to the maximum gradient after comparing each point of the grid with its neighbors. *Miller and Singh (1994)* and *Verduzco et al. (2004)* introduced the tilt angle (TDR) and the total horizontal derivative of the tilt angle (THDR), respectively, which are relatively powerful operators to detect boundaries between areas having a density contrast. The high resolution standardized operators such as the Theta map, horizontal tilt angle (TDX) and E-Tilt, are elucidated by *Wijns et al. (2005)*, *Cooper and Cowan (2006)* and *Muzaffer and Ünal (2013)*, respectively. Despite the high resolution of the derivative operators, the discontinuities and source boundaries derived from their application to the Bouguer anomaly, represent a resultant of different source components seated at different depths. *Fedi and Florio (2001)* presented a multiscale derivative analysis (MDA) based on the enhanced horizontal derivative (EHD). This multiscale analysis allows the determination of source boundaries and discontinuities at different depths.

The first two principal strategies concern themselves with resolving the discontinuities and boundaries of geologic sources while the third is concerned with source characterization. Numerous quantitative interpretations of potential field anomalies are developed after calculation of simple source effects by *Nettleton (1942)*. Despite the complexity of the resolution process caused by the nonlinearity, methods were developed to assess the source parameters from the potential field anomalies as the Werner deconvolution (*Werner, 1953*) and the Euler deconvolution (*Thompson, 1982*).

The latest application was developed by *Reid et al. (1990)* for the interpretation of 2D data. Other applications of Euler deconvolution applied to the analytic signal and the enhanced analytical signal are introduced by *Keating and Pilkington (2004)* and *Salem and Ravat (2003)*, respectively. The source parameters imaging method (SPI) developed by *Thurston and Smith (1997)* is also effective for the evaluation of source parameters of potential field anomalies. The 2D forward modeling of density contrasts at depth has occupied equally an important place in quantitative gravity interpretation studies. The 2D modeling generates geometrical shape and physical properties which provide the closest calculated anomaly to the observed one (*Talwani et al., 1959; Talwani and Ewing, 1960*). However, density contrasts with depth are generally determined using inversion techniques (*Last and Kubik, 1983; Mareschal, 1985; Murthy and Rao, 1993*).

In this paper, we present a multiscale interpretive approach adopted for the three gravity modeling techniques based on the successive decomposition of the Bouguer anomaly. This approach first determines discontinuities and boundaries of sources at different depths in the first step. In the second step, the imaging of density repartition at depth is resolved. This approach was applied to gravity data from northwestern Tunisia with satisfactory results.

2. Processing and methodology

Potential field anomalies are dissociated into residual and regional anomalies using a method of separation. Several pairs of regional and residual anomalies can be obtained from each separation method by changing the director parameter. However, it is possible to separate the Bouguer anomaly into

several components, since it is the sum of the gravity effects of superimposed geological structures situated at different depths. Therefore, several multi-component decomposition scenarios of Bouguer anomaly are possible as the successive decomposition developed by *Arfaoui et al. (2011)*.

Successive decomposition was used to decompose the gravity anomaly with a pseudo-depth slicing scheme (Fig. 1). It was carried out in first step to dissociate the Bouguer anomaly into several pairs of residual and regional anomalies associated with different controlling parameters, which correspond to different pseudo-depths of separation. The second step concerns the dissociation of the residual anomaly corresponding to the pseudo-depth P_i to two anomalies by subtracting the residual anomaly on the pseudo-depth P_{i-1} ($P_{i-1} < P_i$), and we obtained:

– The gravity anomaly of the pseudo-depth slice sited between the pseudo-depths P_i and P_{i-1}.
– Residual anomaly on the P_{i-1} depth.

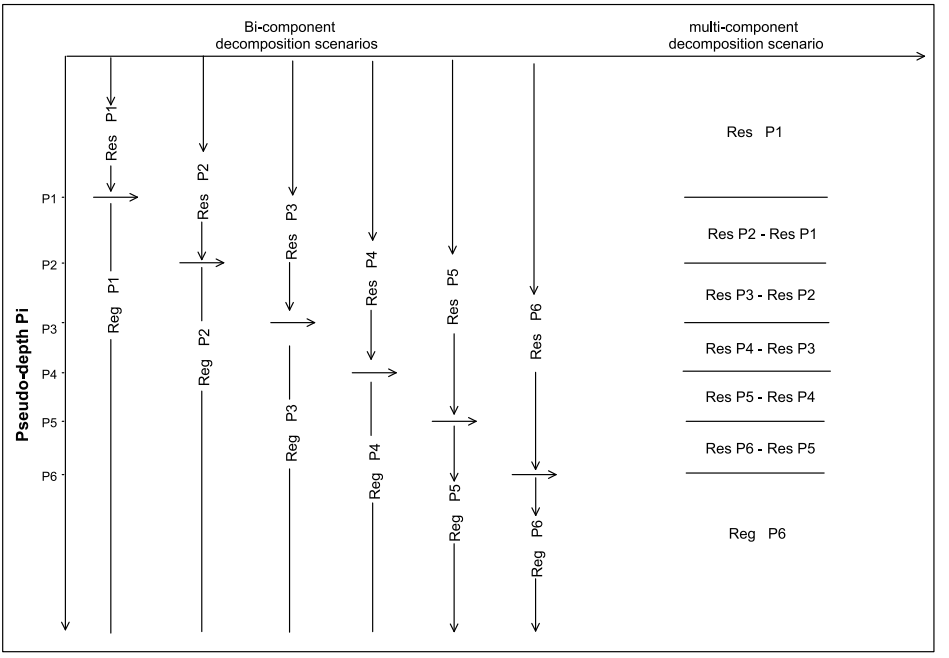

Fig. 1. Successive decomposition of the Bouguer anomaly.

The next steps consist to determining the gravity effects of the pseudo-slice located between the pseudo-depths P_{i-1} and P_{i-2} by the deduction of the residual anomaly corresponding to the pseudo-depth P_{i-2} from the residual anomaly associated to the pseudo-depth P_{i-1}. Thus, the successive decomposition of the Bouguer anomaly using a given separation method, leads to gravity anomalies of several pseudo-depth slices located between the pseudo-depths P_i and P_{i-1}, whose sum is equal to the Bouguer anomaly (Fig. 1).

We decompose the gravity anomaly with a pseudo-depth slicing scheme using the Gaussian filter as a separation method (Fig. 1). Spectral depth analysis in the wavenumber domain (*Spector and Grant, 1970; Negi et al., 1986; Maus and Dimri, 1996; Bansal and Dimri, 2001*) is then used for approximating pseudo-depths of pseudo-slice interfaces. We applied the spectral depth analysis method to estimate depths of the causative sources of anomalies in residual maps associated with standard deviation of Gaussian filter equal 0.4, 0.3, 0.2, 0.1, 0.05 and 0.02 cycle km^{-1}, which approximate the pseudo-depths of pseudo-slice interfaces. The logarithm of the radial average of the energy spectrum of each residual map was plotted versus the radial frequency (Fig. 5). The half slope of each linear segment of the spectrum corresponds to the mean depth of the causative sources of anomalies in the residual maps.

The total horizontal gradient operator is applied to the gravity of pseudo-depth slices derived from the successive decomposition of the Bouguer anomaly to produce horizontal gradient maps at different pseudo-depths. The maxima of this operator correspond to the abrupt density variation zones associated to geological contacts and faults.

The apparent density operator is applied equally to the gravity of pseudo-depth slices to establish apparent density maps at different pseudo-depths from which we evaluate pseudo-density sections. The apparent density operator is performed in the wavenumber domain which assumes that a horizontal layer of fixed thickness and density variable could explain the gravity signal. The operator determines the contrast of the apparent density in the wavenumber domain as expressed in the equation (1) given by *Gupta and Grant (1985)*:

$$L(r) = \frac{r}{2\pi G}\,(1 + e^{-tr})^{-1}\,, \tag{1}$$

where G is the gravitational constant, r is the wavenumber and t is the thickness of the equivalent layer (pseudo-slice). The apparent density maps were calculated by using a thickness equivalent layer equal to the thickness of the pseudo-depth slices. Thus, the thickness of 490, 150, 350, 400, 1210 and 1950 m are used for the gravity anomaly of pseudo-slices 1, 2, 3, 4, 5 and 6 (Fig. 6), respectively. Taking into consideration density values of 350 surface samples and the repartition of outcrops, the background densities of 2.25, 2.28, 2.3, 2.33, 2.38 and 2.42 g/cm^3 are adopted for the calculus of apparent density maps of the pseudo-slices 1 to 6.

The six apparent density maps associated the maps of different slices were used to established density pseudo-slice sections. The apparent density data of each profile are then extracted from the six apparent density maps profiles, combined and attached to pseudo-depths of the anomaly separation interface. After, they are gridded by profile to generate apparent density pseudo-section.

3. Application of the interpretive approach to field case

3.1. Geographic and Geological settings of the study area

The study area is located in the northwestern part of the Tunisian Atlas. It extends from Kalaa El Kasba in the South to Jebel Hairech in the North (Fig. 2).

The study area is located at the front of the nappe zone. It is characterized by folding tectonic, Atlasic type deformation and salt structures. It includes the western parts of three different geological domains: the Mejarda basin in the North, the diapir zone in the middle and the central Tunisian Atlas in the South. Furthermore, the northern part of the study area includes the Permo-Triassic, Triassic, Jurassic and Cretaceous structures, which generally constitute the Mejarda basin limits (Fig. 3). The diapiric zone includes Triassic and Aptian anticlines, Early Eocene synclines and Mio-Pliocene and Quaternary filled depressions. The most notable feature of the southern section is the Kalaa El Khasba through filled with Mio-Plio-Quaternary deposits (*Chihi, 1995*) and the Aptian Recifal limestone outcrops in the form of resistant structures that dominate the relief (*Mahjoubi, 1978; Smati, 1986*). Northwest-southeast and northeast-

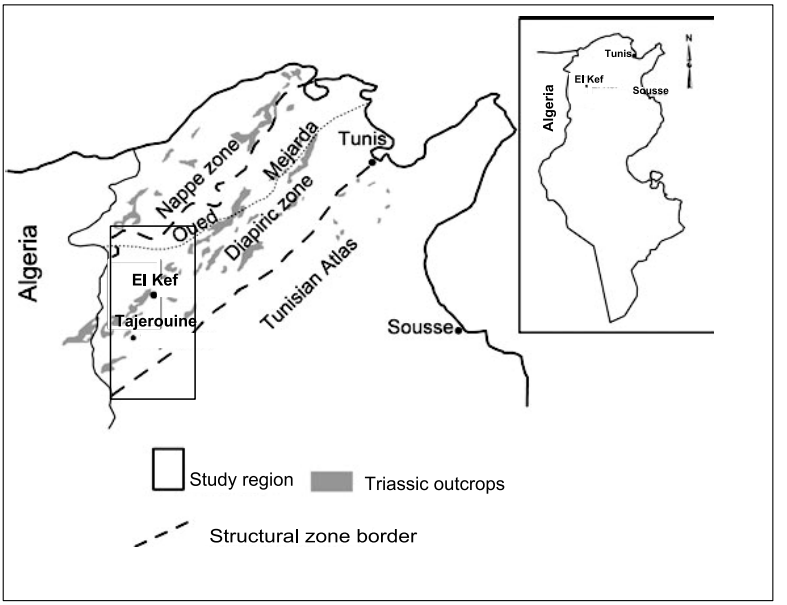

Fig. 2. Location of the study region.

southwest trending faults locally marked by Triassic material, exert control on these structures that are also cut by north-south and east-west trending transverse faults (*Sainfeld, 1951; Burollet and Sainfeld, 1956b; Chikhaoui, 2002; Smati, 1986; Burollet, 1991; Zaier, 1999b; Ould Begga, 2003; Amiri, 2013*). The post-Albian series varies laterally in thickness and facies in response to geodynamic and depositional processes (*Perthuisot, 1978*). Thus, the reduced carbonate series and gaps in the sedimentary sequences may be identified close to Triassic outcrops (Fig. 3). These sequences confirm up-shoaling strata at the emplacement of actual Triassic extrusions (*Perthuisot, 1978; Perthuisot et al., 1998*). Thick and complete sedimentary series with a major marl component are deposited in rim-synclines (Mellègue's dam, Oued Bou Adila area, Jebel Bou Lahnèche and Jebel Jerissa). Since Late Aptian time, the structural evolution of this region has been controlled by successive extensional and compressive tectonic events related to halokinesis (*Perthuisot, 1978; Perthuisot et al., 1998; Chikhaoui, 2002*). The structures comprising basins and Cretaceous up-shoaling were strongly influenced by Tertiary tectonics, thus initiating anticlines, synclines and collapsed troughs.

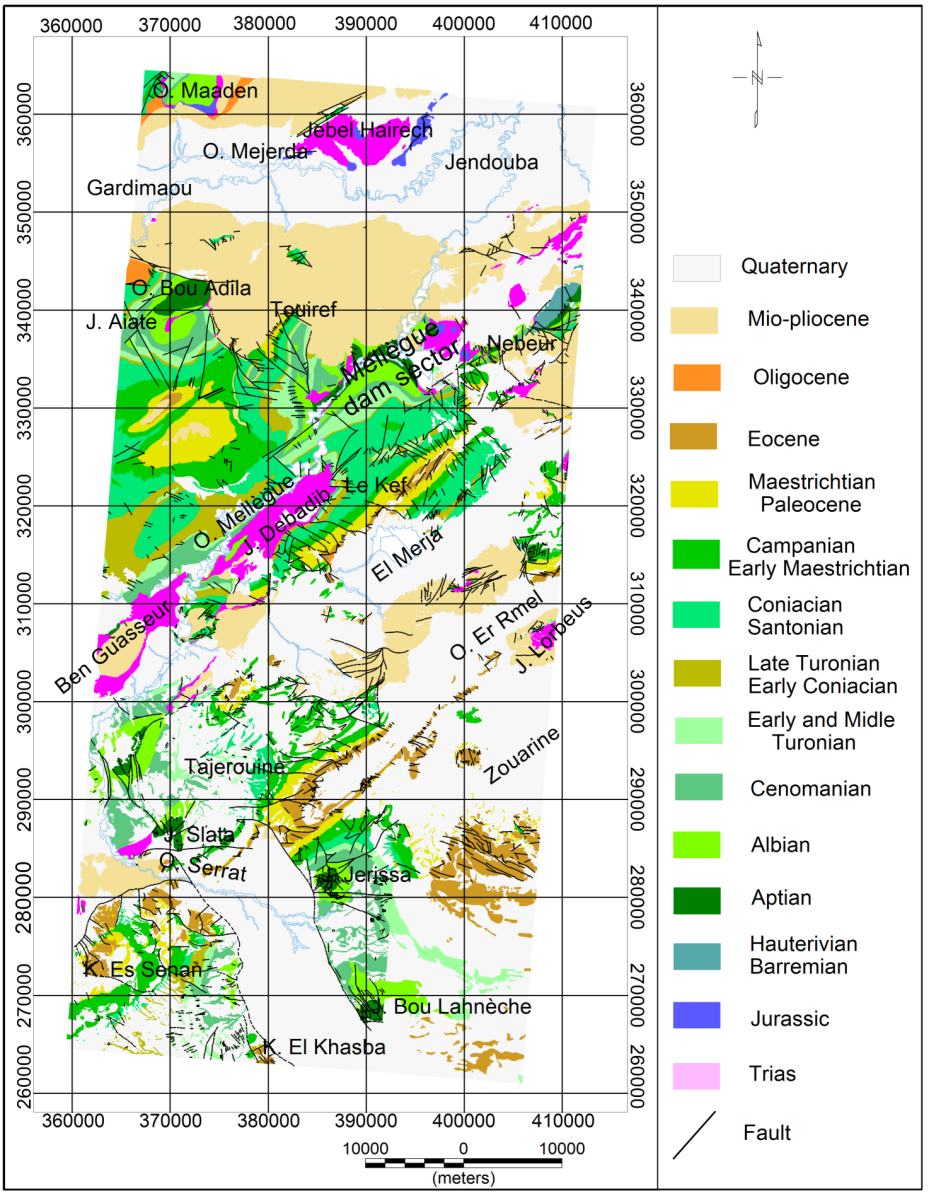

Fig. 3. Geological map of the study region adapted from *Sainfeld (1951), Gottis and Sainfeld (1955), Burollet and Sainfeld (1956a and 1956b), Lehotsky (1979), Lehotsky and Bujnowsky 1995, Ben Haj Ali (1997), Mahjoub (1997), Fakhraoui et al. (1998), Zaier (1999a).*

The main structures (Fig. 3) of the study area are:

- The Mejarda Basin filled by Mio-Pliocene-Quaternary deposits,
- The salt Triassic structures explained by the diapir and salt glacier models (*Ghanmi et al., 2000; Perthuisot et al., 1998; Rouvier et al., 1998; Vila et al., 1994; 1996*),
- The Kef trough sited in the SW Tunisian furrow boundary, is filled by Mio-Pliocene-Quaternary sediments,
- The Kalaa El Khasba trough is a part of the offset graben system of Rohia, Kalaa El Khasba and Ouled Bou Ghanem. It is filled with Mio-Pliocene-Quaternary deposits.

3.2. Gravity anomaly

The Bouguer anomaly represents all mass heterogeneities in depth. Usually the most interesting result from gravity surveys occurs when the survey reveals lineaments that are not observed at the surface. The Bouguer anomaly map also provides important information on the nature of geological structures, and structural directions. A total of 4852 gravity stations from five surveys acquired at 1 km intervals are used in this paper. These gravity surveys belong to a current Tunisia gravity project conducted by the Office National des Mines (Tunisia). It was begun in 1996 as systematic and long term gravity coverage with a 1 station per km^2 for all of Tunisia. Consistent high quality standards in gravity data and elevation control have been maintained since the start of the project. The gravity data acquisition and processing and accuracy standards are described in more detail in previous papers (*Arfaoui et al., 2011; Arfaoui and Inoubli, 2013*).

The Bouguer anomaly map of the study area shows southern and northern domains occupied by long-wavelength negative and positive anomalies, respectively. They are separated by an intermediary domain characterized by short and medium wavelength anomalies (Fig. 4). The northern domain includes the Medjerda Basin and Permo-Triassic, Jurassic and Cretaceous structures of Jebel Hairech and Oued Maaden. It is dominated by long wavelength positive anomalies oriented following E–W and NE–SW directions; with amplitudes ranging between –20 and 13 mGal. Moreover, this domain indicates near surface high density bodies under the Pliocene-Quaternary

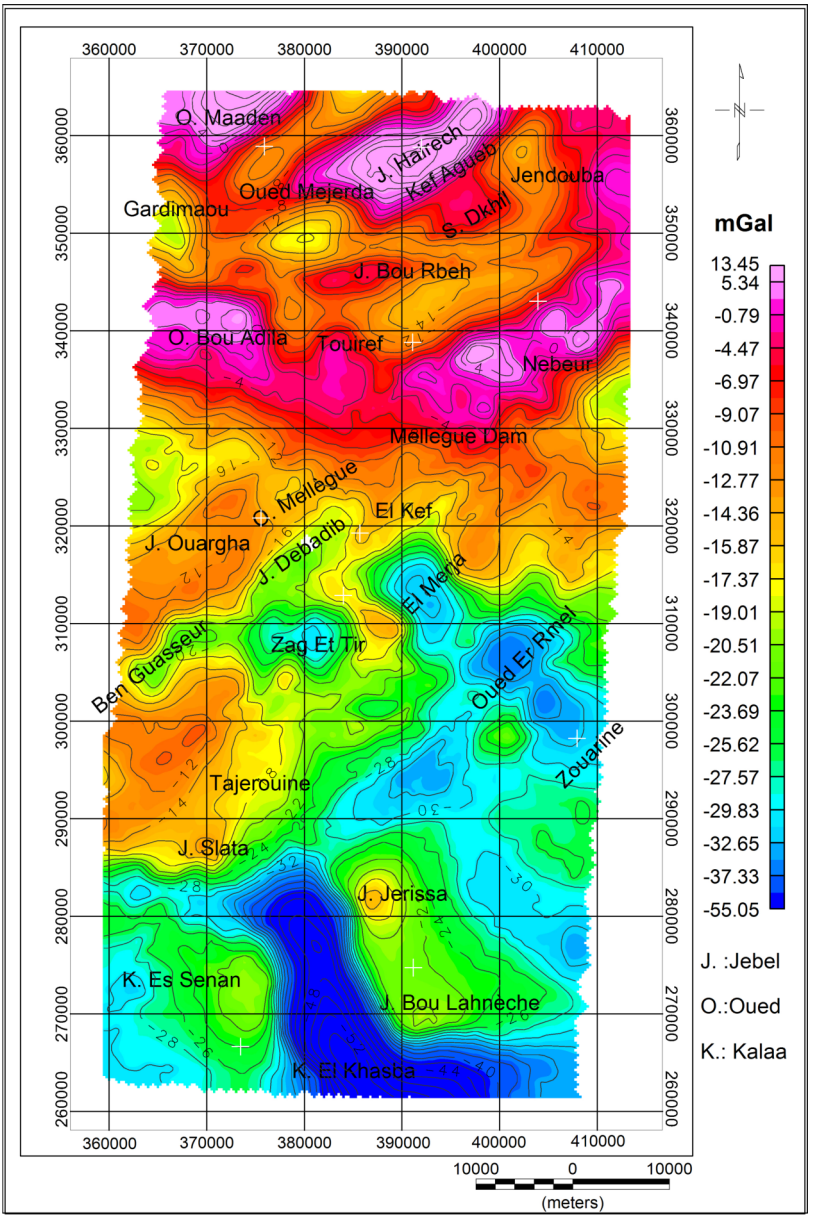

Fig. 4. Bouguer anomaly map.

cover (Fig. 4). The middle domain comprises the Ouargha- El Kef region and its surroundings. It is characterized by short and medium wavelength NE–SW and NW–SE anomalies. It is characterized by positive anomalies coinciding with Quaternary deposits in El Kef and Zouarine plains. They correspond to Cretaceous and/or Eocene structures. The southern domain extends to the south of Tajerouine and is essentially defined by negative

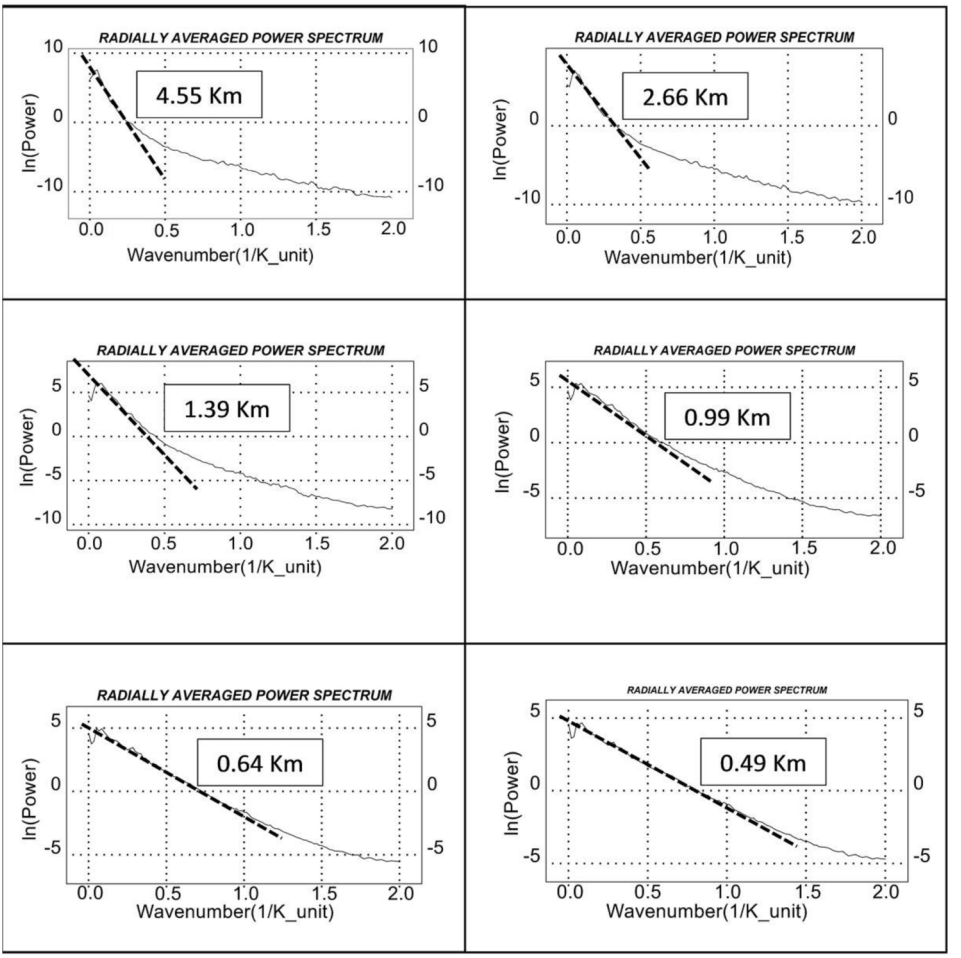

Fig. 5. Radially averaged spectrum of residual maps. Sp Res Gaussian filter 0.3: radially averaged spectrum of the residual map obtained by Residual/ Regional Gaussian filter with standard deviation equal 0.3 cycle km^{-1}.

NW–SE anomalies with amplitudes reaching –55 mGal. The most important one is the Kalaa El Khasba Trough (Fig. 4).

The NW–SE and NE–SW trending gravity lineaments observed on the Bouguer anomaly map correspond to outcropping structures (Kalaa Khasba and El Kef troughs, salt Triassic structures of Jebel Debadib- Ben Gasseur...). They present interruptions and spatial shifts and high gradients along certain anomalies which reflect faults and their effects. The Mio-Plio-Quaternary deposits are associated with two types of anomalies: negative anomalies corresponding to low density material filling collapsed zones and positive anomalies comparable to those observed in the Triassic and Cretaceous series. The positive anomalies are not related to Quaternary deposits but rather support the presence of mass excess. These are attributed to the Triassic and/or Cretaceous and Eocene dense rocks bordering the previously defined collapsed zones. Thus, the positive anomalies situated to the southeast of Jebel Hairech and in the plains of Jendouba and El Kef which coincide with quaternary units are actually caused by denser rocks under the quaternary cover.

In the north, the Jebel Hairech Permo-Triassic and Kef Agueb Jurassic structures belong to a NE–SW positive gravity anomaly which extends to the NE and SW crossing Quaternary units. This confirms the continuity of these structures under the Quaternary overburden. Moreover, the Jebel Hairech structure is bordered by relatively high gradient zones indicating the presence of significant faulting. They appear to have played an important role in the evolution of this structure (Fig. 4). The anomaly amplitudes associated with geological series of same age increase from south to north.

Generally the Bouguer anomaly map explains the majority of mapped outcrops, but it also reveals uncorrelated anomalies, that are probably caused by deeper structures. Resolving the Bouguer anomaly into residual and regional components can resolve the near surface and deeper sources.

3.3. Successive decomposition of the Bouguer anomaly

Successive decomposition of the Bouguer anomaly into several components, using the Gaussian filter as a separation method, allows the review of mainly structural features and the analysis of density variation in depth (Fig. 6). The regional anomaly derived from the Gaussian filter of standard deviation

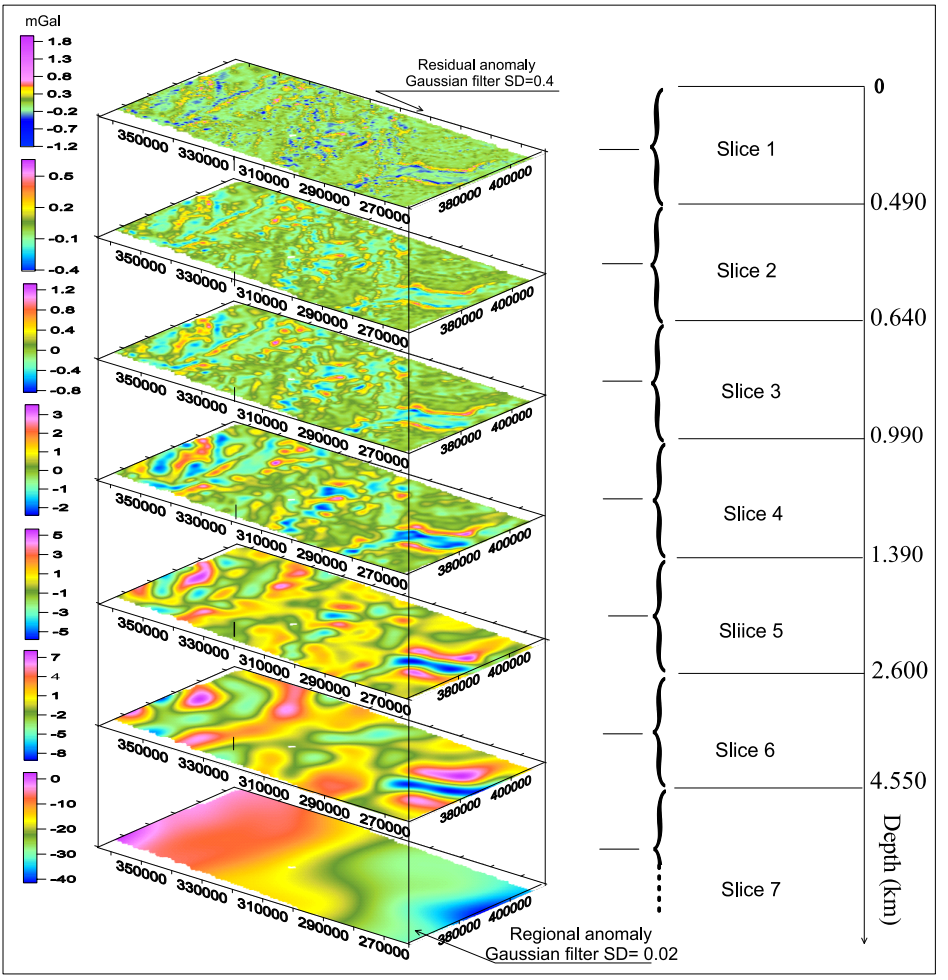

Fig. 6. Successive decomposition of Bouguer anomaly, using the Gaussian filter.

equal to 0.02 cycle km^{-1}, shows a general linear trend extending from NNW to SSE. The northern zone is dominated by a general gravity high oriented east-west while the southern zone is characterized by a gravity low oriented NW–SE. Those zones are separated by a middle region characterized by an arch shaped high gradient following the NE–SW direction (Fig. 6). The analysis of the pseudo-depth sliced gravity shows an increase in the size of the anomalies and an attenuation of certain anomalies with depth.

The pseudo-depth slices 1, 2 and 3 correlate with the pseudo-depths of 0–490, 490–640, and 640–990 m, respectively. Their gravity effects show dominate anomaly directions: E–W in the north, NW–SE and NE–SW in the center and NW–SE in the south (Fig. 6). They show equally:

- An anomaly shape smoothing with depth; thus, the positive anomaly of Sidi Dkril located in the East of Jebel Hairech and between Oued Mejarda and Oued Mellègue, is composed of two anomalies on the pseudo-depth slices 1 and 2, which merge into one in the pseudo-depth slice 3. This expresses the gravity effect of a near surface fault affecting the source of this anomaly but the lack of its persistence with depth suggests it is not a major fault.
- Good correspondence between gravity anomalies and outcropping series despite the exception of the uncorrelated anomalies observed in the Mio-Pliocene and quaternary deposits. This correspondence shows a general continuity of those outcropping series in depth to a pseudo-depth of 1000 m.
- Negative anomalies are associated with the Triassic outcrops of Jebel Aiate (Oued Bou Adila), Jebel Debadib- Ben Gasseur and Mellegue dam sector while other Triassic outcrops in the study area are associated with positive anomalies.
- Positive anomalies occur within Mio-Plio-Quaternary deposits of Mejarda basin. They extend for several kilometers along the E–W and NE–SW directions. They seem to be related to dense materials similar to Triassic, Jurassic and Cretaceous outcropping series, under thin Mio-Plio-Quaternary overburden. This suggests the Mejarda basin is more complex than a simple structural collapse basin. Notice in particular that positive anomalies attenuate significantly with pseudo-depth greater than 2 km (Slice 5 of Fig. 6).

The pseudo-depth slices 4, 5 and 6 correspond to the pseudo-depth ranges: 990 to 1390, 1390 to 2600 and 2600 to 4550 m, respectively. The gravity maps associated with these slices are characterized by NW–SE and NE–SW anomalies which become more dominant at greater depths (Fig. 6). The pseudo-depth slices 4, 5 and 6 show:

- All anomalies associated with outcrop structures are totally attenuated from the slice 5 or a pseudo-depth equal to 2600 m. Thus, the negative

anomalies on the Triassic outcrops of Jebel Aiate (Oued Bou Adila) and Mellegue dam sector disappear at the pseudo slice 4, indicating a vertical continuity of Triassic outcrop materials to a pseudo-depth equal to 1400 m. The negative anomaly associated with salt Triassic outcrops of Jebel Ben Debadib- Gasseur disappears completely at the pseudo-depth slice 5. This suggests that these outcrops are rooted to a pseudo-depth of 2600 m.

- A progressive attenuation with depth of NW–SE negative anomalies associated to El Marja, Oued Er Rmel and Zouarin basins. By pseudo-depth slice 5 they are reduced to one single anomaly. A similar effect is observed in the El Kef Plain, where the succession of positive and negative anomalies associated with high and collapsed zones continue to pseudo-depth slice 4; this succession is represent by a negative anomaly in the gravity map of slice 5.
- Positive anomalies associated with dense structures under Mio-Plio-Quaternary deposits attenuate with depth until they disappear entirely.
- The NW–SE anomalies of the middle domain are continuous with depth. For pseudo- depth slices 1 through 4, the NE–SW trends have more continuity and they truncate the NW–SE trends. But for depth slices 5 and 6, the NW–SE trend truncate the NE–SW anomalies.

3.4. Multiscale discontinuities and boundary identification

Next, the total horizontal gradient filter is applied to the gravity anomalies of pseudo-depth slices resulting from the successive decomposition of Bouguer anomaly. This permits identification of abrupt density variation zones with depth (Fig. 7). The total horizontal gradient of the gravity anomaly of deeper slice (7) (regional anomaly determiner with the Gaussian filter of standard deviation equal to 0.02 cycle km^{-1}) shows discontinuities of density for depths greater than 4550 m. It shows an important NW–SE discontinuity which corresponds with the deep fault identified by *Arfaoui et al. (2015)*. This fault cuts a NE–SW fault to the east of El Kef. These are the dominant structural directions at depth for this study area and show no correlation with the Triassic outcrops at the surface. But for the pseudo-depth slice 6 (2600 m) some of the surface faults begin to become apparent.

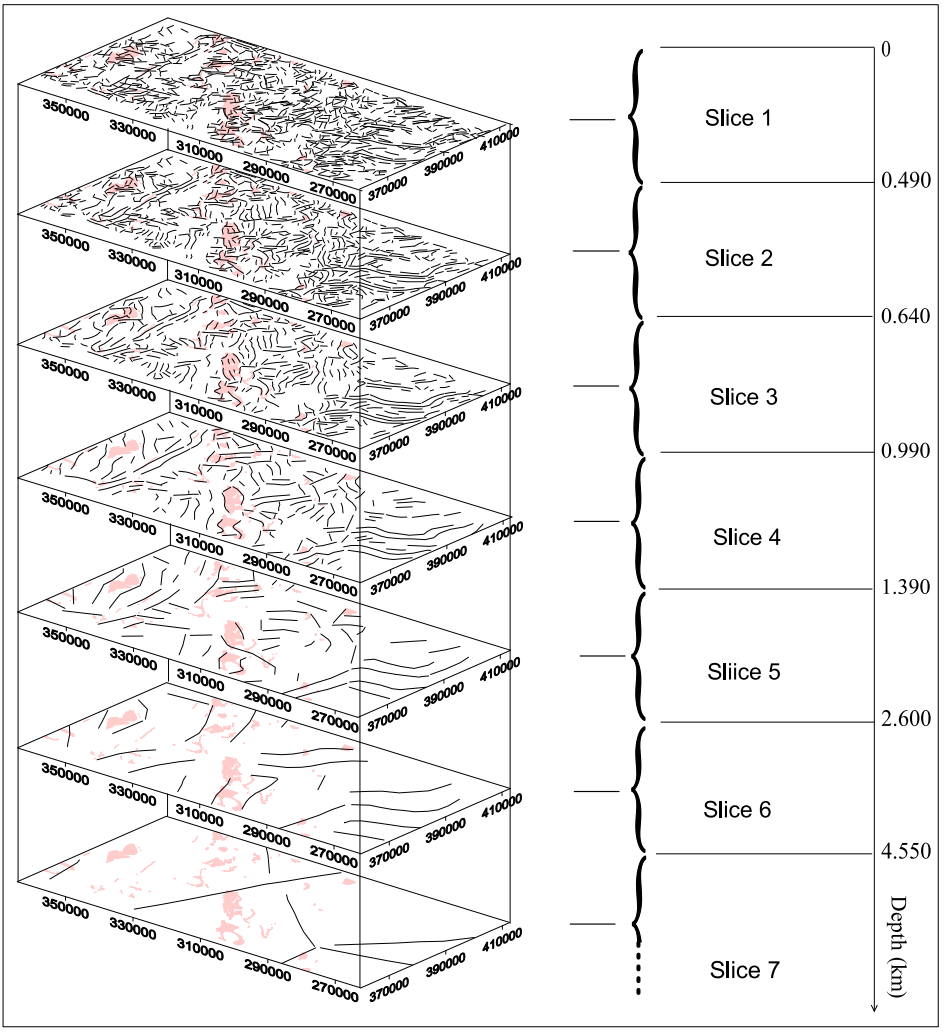

Fig. 7. Multiscale discontinuities and boundaries derived from the total horizontal gradient. Triassic outcrops is indicate in red color.

For example, the border faults of El Kalaa Khasba trough, the north fault oriented E–W that ties this trough to the Ouled Boughanem trough, the two faults limiting the Jebel Hairech structure, and the faults constituting the southern limit of the Mejarda basin all show some expression (Fig. 7). Both areas of the high total horizontal gradient surround the Ben Gasseur

Triassic structure; they indicate zones of abrupt density variations at this depth. Besides, they provide the Triassic series disturbance in this area. At this pseudo-depth the NW–SE fault is interrupted at El Kef apparently as a result of the Triassic materials rising. The NW–SE and NE–SW structural directions are still dominant over the middle domain structures (Fig. 7).

The pseudo-depth slice 5 (1400 m) shows:

- The south fault between the Ouled Boughanem and El Kalaa Khasba troughs. This south fault is relatively shallower than the northern fault, whose direction is close to E–W.
- N–S faults affecting the NW–SE and NE–SW fault of the southern border of Mejarda basin and the E–W faults that begin to appear in this basin.
- The NE–SW faults affect NW–SE faults in the middle domain. This is more indication of the change in the direction of the dominant faults mentioned previously.
- The strike-slip faults limiting the structures of Jebel Hairech, Kef El Jebel Agab and Chouichia, which evolved particularly to the SE.
- The discontinuities bordering the Ben Guasseur Triassic structure extend northwards towards Jebel Debadib. Extension of this area to the east is highly probable including the Zag Et Tir sector. Similarly, the bounding faults of the Sidi Dkril positive gravity anomaly in SE of Jebel Hairech appear to extend to this depth.

At the pseudo-depth slice 4 (1000 m), NE–SW faults dominate structures in the middle domain. They cut the NW–SE faults, especially on the emplacement of the deep NW–SE fault. The deepest NW–SE fault cuts a NE–SW fault at depth (slice 7), but at shallower depths (slice 4, 3.) the fault systems are changing. NE–SW discontinuities affect the NW–SE discontinuities suggesting a change of tectonic regime or a variation of its main direction.

At this pseudo-depth (1000 m), Triassic outcrops of Jebel Debadib including Ben Gasseur, the Mellègue Dam sector and Jebel Aiate (Oued Bou Adila) are clearly outlined by zones of maximum total horizontal gradient reflecting the vertical continuity of these structures. The two parallel E–W discontinuities in the Mejarda basin extend to the east for a greater distance. The bounding faults of the Jebel Hairech structure appear to be effected by other NE–SW faults. NW–SE faults begin to manifest in El Kalaa Khasba

trough (Fig. 7).

Moving to pseudo-depth slices 3 and 2 (less than 650 m), we see an increase in the number of discontinuities with a decrease of their lengths. With the exception of the bounding faults of El Kalaa El Khasba trough, all the faults discussed previously are cut by other faults. These include:

- The E–W Faults limiting Jebel Hairech that are affected by NE–SW and NW–SE faults.
- The E–W faults of Mejarda Basin.
- The faults bordering mini-basins of El Merja, Oued Er Rmel and Zouarine.
- The faults of E–W branch depression linking the El Kalaa El Khasba and Ouled Boughanem troughs.

Thus, the middle domain is characterized by two fault types differentiated by their directions: NE–SW and NW–SE. The NE–SW faults are the most dominant and they affect the NW–SE ones. Compared to the middle and southern domains, the northern domain is characterized by deep quiet structures that influenced by the activity of the EW and NE–SW faults at relatively superficial depth (Fig. 7). The multi-scale analysis using the total horizontal gradient of gravity slices allows for delineation of faults or geological contacts.

3.5. Apparent density pseudo-section derived from successive decomposition

The apparent density operator is applied generally, to generate density maps (*Gupta and Grant, 1985; Granser et al., 1989; Gupta and Sutcliffe, 1990; Keating, 1991; Singh et al., 2003; Arfaoui et al., 2011*). In our case we applied this operator to the gravity anomalies of pseudo-depth slices resulting from the successive decomposition of Bouguer anomaly, to generate density maps of pseudo-depth slices.

The process used to evaluate pseudo-sections describing density distribution at depth, consisted on the extraction of the apparent densities data of each profile from the apparent density maps and the attribution of a pseudo depth of the anomaly separation interface to these data. After, they are gridded by profile to generate apparent density pseudo-section.

Five isolated profiles of apparent density pseudo-sections are selected to examine important structural features (Fig. 8). The profiles adopted for this approach cross the mainly geologic structures of the study area: Mejarda Basin, salt structure of Jebel Debadib, El Marja-Oued Er Rmel and Zouarine basins and The Kalaa El Khaba through. The pseudo-sections PI and PII cross the positive and negative Bouguer anomalies of Mejarda basin. They show the presence of dense structures under the Mio-Plio-Quaternary overburden.

Indeed, the Sidi Dkril Bouguer anomaly is associated with a dense structure whose density varies between 2.38 and 2.48 g/cm^3. It is covered by deposits of 500 m thickness and a density ranging between 2.24 and 2.28 g/cm^3, (Fig. 9).

Two other high zones are located northwest of Oued Mliz and at Jebel Bou Rbah. They are covered by 500 m of Mio-Plio-Quaternary. However, the Oued Mliz and Oued Rarai areas and the southeastern part of Jebel Bou Rbah are characterized by thick Pliocene-Quaternary deposits with 2000 m of thickness (Fig. 10). The presence of Cretaceous and Eocene series at the base of collapsed zones is possible, especially since the density ranges between 2.34 to 2.36 g/cm^3. Directly below the high zones, the density decreases between 2000 and 4000 m depth (Fig. 10).

The pseudo-section density passing through Jebel Debadib shows a low density diapir shape with a rooting depth of 2000 m and a width of 4000 m (Fig. 11). At surface the density decreases from west to east (2.30 g/cm^3 to 2.23 g/cm^3), reflecting the heterogeneity of Triassic materials in this part of the diapir compared to the basal of the diaper portion that is homogeneous with a density less than 2.23 g/cm^3 (Fig. 11). The basal part of the diapir shows a Triassic series dip to the southeast which could explain the reduction of the rooting depth (1000 m) revealed previously in the Triassic outcrops of Jebel Aiate and Mellègue dam sector located further in the north.

The pseudo-density section of profile IV shows the structures of successive mini-basins of El Merja, Oued Rmel and Zouarine. It indicates an overburden of densities less than 2.28 g/cm^3 with thicknesses varying between 500 and 800 m. This overburden consisting of Mio-Pli-Quaternary deposits hides relatively dense terrains (2.32 g/cm^3) that are attributed to Eocene and Cretaceous rocks (Fig. 12).

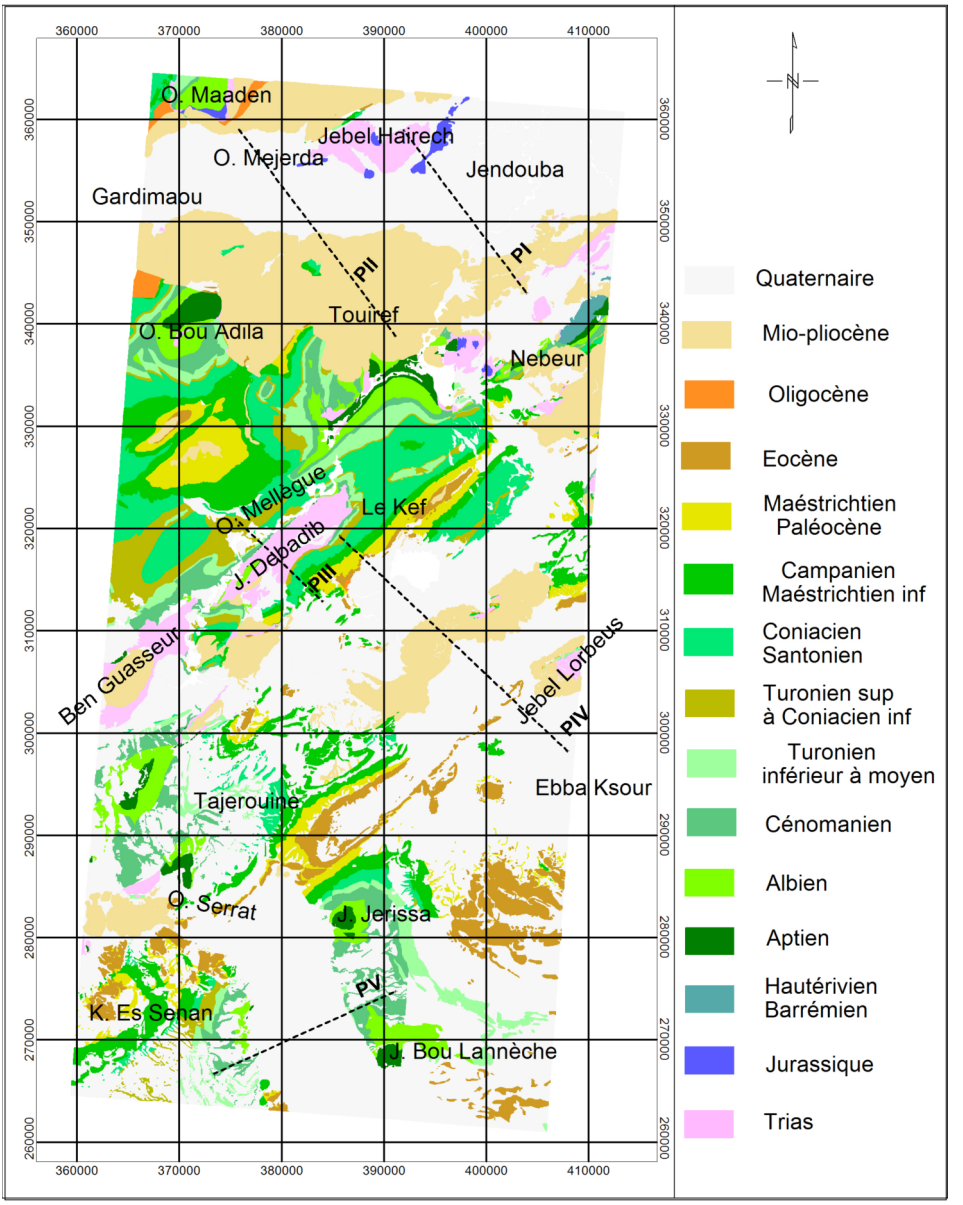

Fig. 8. Location of profiles used for the pseudo-section density imaging.

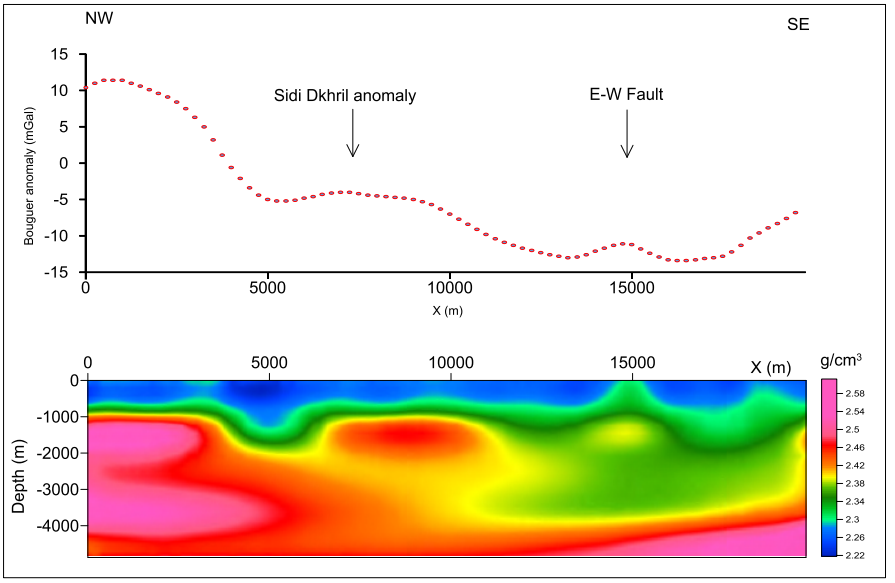

Fig. 9. Pseudo-section density of profile PI, Mejarda basin.

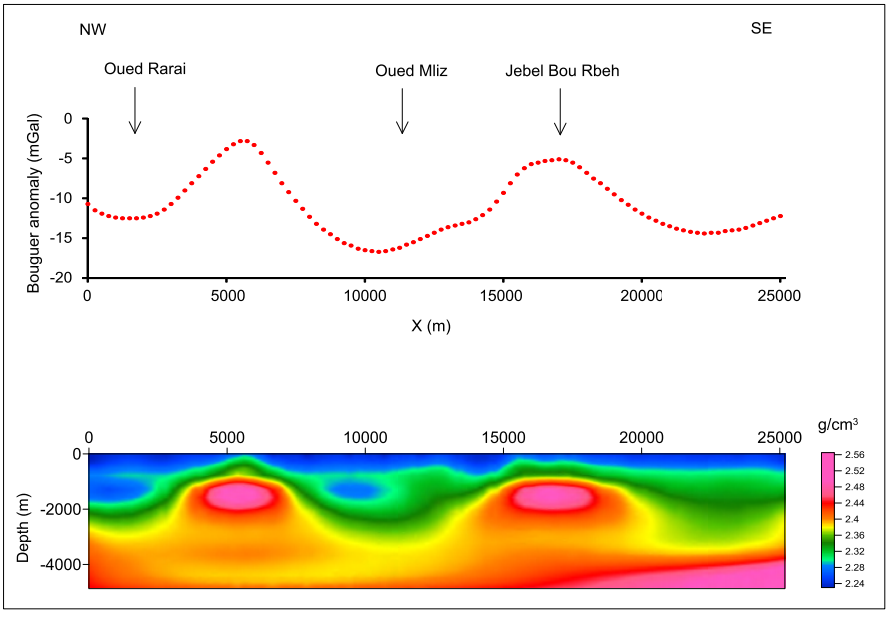

Fig. 10. Pseudo-section density of profile PII, Mejarda basin.

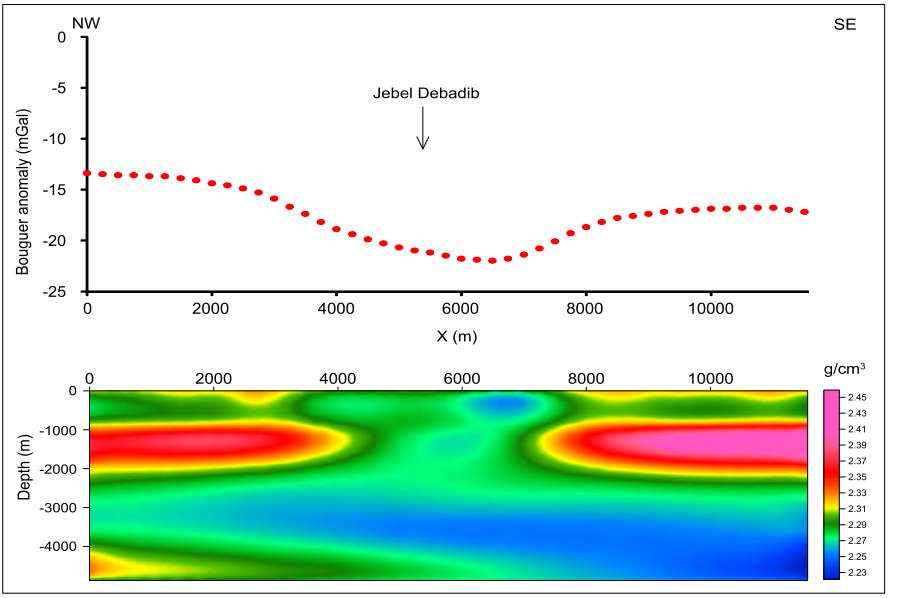

Fig. 11. Pseudo-section density of profile PIII, salt structure of Jebel Debadib.

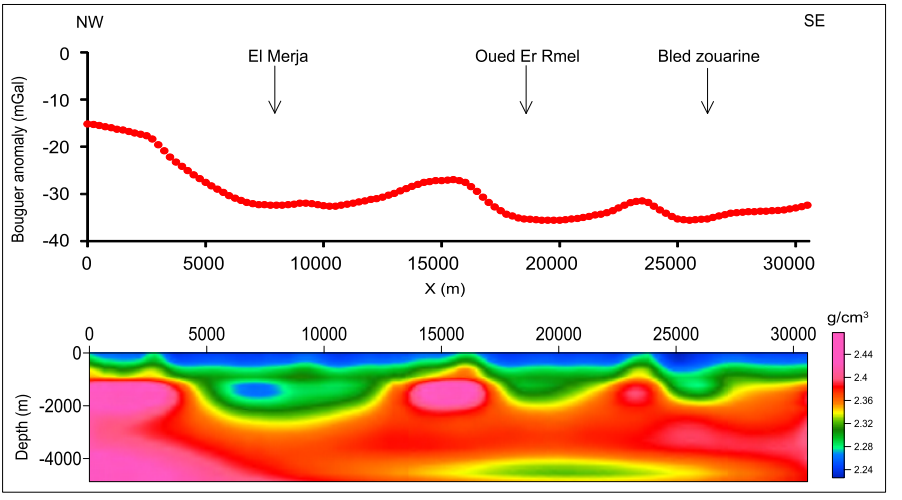

Fig. 12. Pseudo-section density of profile PIV, successive basins El Marja, Oued Er Rmel and Zouarine.

The distribution of the density in El Kalaa Khasba trough shows terrains of low density at the center (2.25 g/cm^3) traversed by relatively dense series (2.35 g/cm^3) at a depth of 1000 m (Fig. 13). This distribution could indicate the presence of Cretaceous and Triassic materials at depth. The density distribution also shows the bounding faults dip towards the center of the trough and that they are stopped at 2500 m depth. At this point two contacts appear to reverse toward the west and the east. These contacts combined with the density distribution beyond a depth of 2500 m, provide the appearance of a dome having two clearly distinguishable horizons defined by their densities. The deeper horizon sited at a depth greater than 4000 m has a density equal to 2.28 g/cm^3; it is surmounted by a dense horizon (2.34 g/cm^3), between the depths of 3500 m and 2500 m (Fig. 13). The dome seems to be Triassic, and agrees with the rise of Triassic materials started during the primary stages of formation of the Kalaa El Khasba trough (*Lehotsky and Bujnowsky, 1995*).

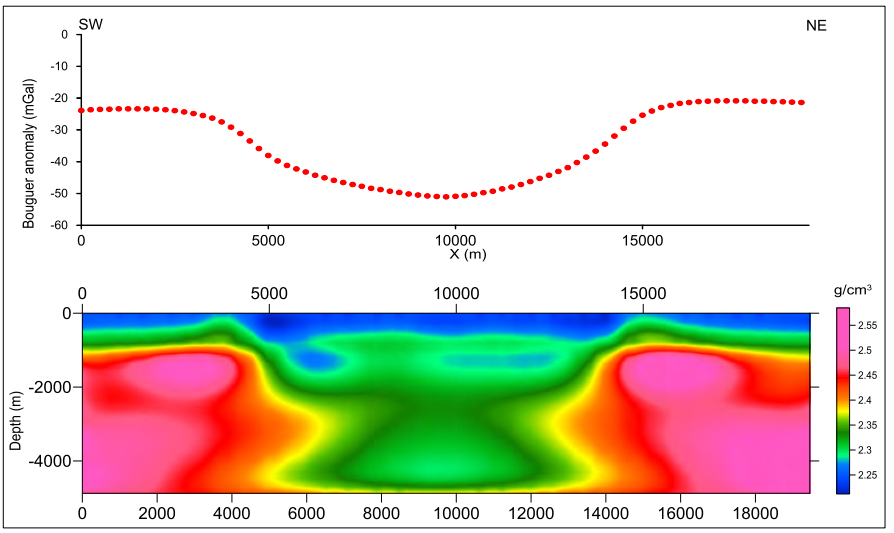

Fig. 13. Pseudo-section density of profile PV, Kalaa El Khasba.

4. Accuracy of the Results

The gravity of pseudo-slices available by the successive decomposition of Bouguer anomaly can be adopted to identify the discontinuities and geo-

logic contacts at different depths and to image density repartition on depth. These constitute a rapid interpretive approach improved by the total horizontal gradient and the apparent density operators. The results obtained correlate with the majority of surface geologic units and model the gravity structure effect as a density distribution following pseudo-section density. However, certain sources of error associated with this approach can cause discrepancies in results, as the depths of pseudo-slices and the background density used to calculate the apparent density maps. Depths of pseudo-slices are approximated by the spectral depth analysis method which corresponds to mean depths of the causative sources of anomalies in residual maps. However, the causative sources associated with the residual anomalies exist at different depths.

The densities used for transforming the gravity maps of pseudo-slices to apparent density maps are chosen from the values of measured density of surface rocks since we have no other control data. Background densities adopted are chosen as an increasing function with depth, but they remain a source of error which affects only the values of densities in the pseudo-depth sections. They do not affect the image of geologic structure in the pseudo-depth section resulting from the repartition of density since as the apparent density operator calculates a contrast of density independently of the background density, which is added at the end of the process as an average density.

Certainly, the resolution of the pseud-sections density and witch of multiscale discontinuities are affected by errors caused by the assessment process of depth and density. Taking into consideration the gravity survey scale (1/50000) and the spacing inter stations (1 km), we think that the results reflect regional model with an acceptable resolution accuracy ratio of the interpretative approach.

5. Conclusion

The multiscale interpretive approach based on the pseudo-depth slice gravity anomalies derived from the successive decomposition of Bouguer anomaly generally provided acceptable results compared to structural geological models in the study area. The use of depth spectral analysis makes this interpretive approach more capable of revealing the evolution of fault systems

and causative source boundaries with depth and equally to establish 2D pseudo-section density. The multiscale approach reveals deeper NW–SE and NE–SW faults compared to the relatively superficial N–S and E–W faults. It indicate that the excess of mass anomaly presented by the basins of the study correspond to Triassic, Cretaceous and/or Eocene dense rocks sited at relatively shallow depth under the Mio-Pliocene and Quaternary deposits. The salt Triassic outcrops of Jebel Debadib provide a diapir model with a homogeneous basal layer dipped to southeast. The basement under the Kalaa El Khasba trough is a Triassic dome.

Acknowledgements. We would like to express our thanks to the Office National des Mines (Tunisia) for permission to use the gravity data of the study region. Many thanks also to the technical editor and reviewer for their constrictive suggestions that improved the final version of this manuscript substantially.

References

Amiri A., 2013: Apport de la géophysique appliquée à la modélisation géodynamique de la moyenne valée de Mejarda. PhD. Thesis., Université Tunis El Manar, Faculté des sciences de Tunis (in French).

Arfaoui M., Inoubli M. H., Tlig S., Alouani R., 2011: Gravity analysis of salt structures. An example from the El Kef-Ouargha region (northern Tunisia). Geophysical Prospecting, **59**, 576–591.

Arfaoui M., Inoubli M. H., 2013: Advantages of using the kriging interpolator to estimate the gravity surface, comparison and spatial variability of gravity data in the El Kef-Ouargha region (northern Tunisia). Arabian Journal Geosciences, **6**, 3139–3147.

Arfaoui M., Reid A., Inoubli M. H., 2015: Evidence for a new regional NW–SE fault and crustal structure in Tunisia derived from gravity data. Geophysical Prospecting, **63**, 1272–1283.

Bansal A. R., Dimri V., 2001: Depth estimation from the scaling power spectral density of nonstationary gravity profile. Pure and Applied Geophysics, **158**, 799–812.

Ben Haj Ali M., 1997: Carte géologique au 1/50000 de Jendouba. Feuille No 32. Office National des Mines. Tunisie.

Blakely R. J., Simpson R. W., 1986: Approximating edges of source bodies from magnetic or gravity anomalies. Geophysics, **51**, 1494–1498.

Burollet P. F., 1991: Structures and tectonics of Tunisia. Tectonophysics, **195**, 359–369.

Burollet P. F., Sainfeld P., 1956a: Carte géologique au 1/50 000 d'El Kef. Direction des Mines et de la Géologie. Tunisie.

Burollet P. F., Sainfeld P., 1956b: Carte géologique au 1/50 000 de Tajerouine. Feuille No 50. Direction des Mines et de la Géologie. Tunisie.

Chihi L., 1995: Les fossés néogènes à quaternaires de la Tunisie de la mer pélagienne: leur signification dans le cadre géodynamique de la méditerranée centrale. PhD. Thesis., Université de Tunis El Manar (in French).

Chikhaoui M., 2002: La zone des diapirs en Tunisie: Cadre structural et évolution géodynamique de la sédimentation méso-cénozoïque et géométrie des corps triasiques. PhD. Thesis., Université de Tunis el Manar (in French).

Cooper G. R. J., Cowan D. R., 2006: Enhancing potential field data using filters based on the local phase. Computers & Geosciences, **32**, 1585–1591.

Cordell L., Grauch V. J. S., 1982: Mapping basement magnetization zones from aeromagnetic data in the San Juan Basin New Mexico. Presented at the Snd. Ann. Internat. Mtg. Sot. Explor. Geophys. Dallas, abstracts and biographies, 246–247.

Cordell L., Grauch V. J. S., 1985: Mapping basement magnetization zones from aeromagnetic data in the San Juan basin New Mexico. In Hinze W. J. Ed. The utility of regional gravity and magnetic anomaly maps Sot. Explor. Geophys, 181–197.

Fakhraoui M., Ghanmi M., Hatira N., 1998: Carte géologique au 1/50.000 De Nebeur. Feuille No 39. Office National des Mines. Tunisie.

Fedi M., Florio G., 2001: Detection of potential fields source boundaries by enhanced horizontal derivative method. Geophysical Prospecting, **49**, 40–58.

Ghanmi M., Vila J. M., Ben Youssef M., Jouirou M., Ben Kherouf F., 2000: Le matériel triasique interstratifié dans l'Albien de l'anticlinal autochtone atlasique du Jebel Takrona (Tunisie): Stratigraphie Arguments gravimétriques signification dans la transversale N–S des confins algéro-tunisiens (Maghreb du Nord-Est). Bulletin Sciences Histoires Naturelles, **136**, 19–27 (in French).

Gupta V. K., Ramani N., 1980: Some aspects of regional-residual separation of gravity anomalies in a Precambrian terrain. Geophysics, **45**, 1412–1426.

Gottis C., Sainfeld P., 1955: Carte géologique au 1/50.000 de Ghardimaou. Feuille No 31. Direction des Mines et de la Géologie. Tunisie.

Gupta V. K., Grant F. S., 1985: Mineral exploration aspects of gravity and aeromagnetic surveys in the Sudbury-Cobalt area, Ontario. SEG; The Utility of Regional Gravity and Magnetic Anomaly Maps, W. J. Hinze (Editor), 392–411.

Gupta V. K., Sutcliffe R. H., 1990: Mafic-ultramafic intrusives and their gravity field: Lac des Iles area, northern Ontario. Geological Society of America Bulletin, **102**, 1471–1483.

Granser H., Meurers B., Steinhauser P., 1989: Apparent density mapping et 3D gravity inversion in the eastern Alps. Geophysical Prospecting, **37**, 225–330.

Keating P., 1991: Density mapping from gravity data using Walsh transform. Geophysics, **57**, 637–642.

Keating P., Pilkington M., 2004: Euler deconvolution of the analytic signal and its application to magnetic interpretation. Geophysical Prospecting, **52**, 165–182.

Last B. J., Kubik K., 1983: Compact gravity inversion. Geophysics, **48**, 713–721.

Lehotsky I., 1979: Carte géologique au 1/50.000 d'Ebba Ksour. Feuille No 52. Office National des Mines. Tunisie.

Lehotsky I., Bujnowsky A., 1995: Carte géologique au 1/50.000 de Kalaat Es Senan. Feuille No 59. Office National des Mines. Tunisie.

Mahjoub K., 1997: Carte géologique au 1/50.000 de Les Salines. Feuille No 45. Office National des Mines. Tunisie.

Mahjoubi H., 1978: Un exemple de gisement ferrifère en un milieu recifal, Jerissa (Tunisie). PhD. Thesis., Univesité de Tunis.

Mareschal J. C., 1985: Inversion of potential field data in Fourier transform domain. Geophysics, **50**, 685–691.

Maus S., Dimri V., 1996: Depth estimation from the scaling power spectrum of potential fields? Geophysical Journal International, **124**, 113–120.

Miller H. G., Singh V., 1994: Potential field tilt – A new concept for location of potential field sources. Journal of Applied Geophysics, **32**, 213–217.

Murthy I. V. R., Rao P. R., 1993: Inversion of gravity and magnetic anomalies of two-dimensional polygonal cross sections. Computer Geosciences, **19**, 1213–1228.

Muzaffer O. A., Ünal D., 2013: Edge detection of magnetic sources using enhanced total horizontal derivative of the tilt angle. Bulletin of the Earth Sciences Application and Research, Centre of Hacettepe University.

Negi J. G., Dimri V. P., Agrawal P. K., Petey O. P., 1986: A spectral analysis of the profiles for thickness estimation of flood basalt of India. Exploration Geophysics, **17**, 105–111.

Nettleton L. L., 1942: Gravity and magnetic calculation. Geophysics, **7**, 293–310.

Ould Begga M. A., 2003: Evolution tectono-sédimentaire et analyse structural d'un segment des magrébides orientales: la région de Ghardimaou-Fernana (Tunisie Nord occidentale). PhD. Thesis., Université El Manar, Faculté des sciences de Tunis (in French).

Pawlowsky R. S., Hansen R. O., 1990: Gravity anomaly separation by Wiener filtering. Geophysics, **55**, 539–548.

Perthuisot V., 1978: Dynamique et pétrogenèse des extrusions triasiques en Tunisie septentrionale. PhD. Thesis., Ecole Normale Supérieure Paris (in French).

Perthuisot V., Aoudjehane M., Bouzenoune A., Hatira N., Laatar E., Mansouri A., 1998: Les corps triasiques des monts du Mellègue (confins algéro – tunisiens) sont-ils des diapirs ou des "glaciers de sel". Bulletin de la Société géologique de France, **169**, 53–61 (in French).

Reid A. B., Allsop J. M., Granser H., Millett, A. J., Somerton I. W., 1990: Magnetic interpretation in three dimensions using Euler deconvolution. Geophysics, **55**, 80–91.

Rouvier H., Henry B., Le Goff M., Hatira N., Laatar E., Mansouri A., 1998: Preuves paléomagnétiques de la non-interstratification des évaporites du Trias dans l'Albien du Maghreb oriental. Comptes Rendus de l'Académie des Sciences, **326**, 363–368 (in French).

Sainfeld P., 1951 : Carte géologique au 1/50000 d'Ouargha. Feuille No 38. Direction des travaux publics. Tunisie.

Salem A., Ravat D., 2003: A combined analytic signal and Euler method (AN-EUL) for automatic interpretation of magnetic data. Geophysics, **68**, 1952–1961.

Simpson S. M., 1954: Least- squares polynomial fitting to gravitational data and density plotting by digital computer. Geophysics, **19**, 808–811.

Singh A. P., Michra D. C., Axman G., 2003: Apparent density mapping and 3D gravity inversion of Dharwar crustal province. Journal of Indian Geophysical Union, **7**, 1–9.

Smati A., 1986: Les Gisements de Pb-Ba et de Fe du Jebel Slata (Tunisie du centre-nord) : minéralisations épigénétiques dans le crétacé néritique de la bordure d'un diapir de Trias, gisements de Sidi Amor Ben Salem et de Slata-Fer. PhD. Thesis., Université Pierre et Marie Curie Paris VI (in French).

Spector A., Grant F. S., 1970: Statistical models for interpreting aeromagnetic data. Geophysics, **35**, 293–302.

Talwani M., Worzel J. L., Letisman M., 1959: Rapid gravity computations for twodimensional bodies with application to the Mendocino submarine fracture zone. Journal of Geophysical Research, **64**, 49–59.

Talwani M., Ewing M., 1960: Rapid computation of gravitational attraction of threedimensional bodies of arbitrary shape. Geophysics, **25**, 203–225.

Thompson D. T., 1982: EULDPH: A new technique for making computer assisted depth estimates from magnetic data. Geophysics, **47**, 31–37.

Thurston J. B., Smith R. S., 1997: Automatic conversion of magnetic data to depth, dip, susceptibility contrast using the SPI^{TM} method. Geophysics, **62**, 807–813.

Verduzco B., Fairhead J. D., Green C. M., Mackenzie C., 2004: New insights into magnetic derivatives for structural mapping. The Leading Edge, **23**, 116–119.

Vila J. M., Ben Youssef M., Charriere A., Chikhaoui M., Ghanmi M., Kamoun F., 1994: Découverte en Tunisie, au SW du Kef, de matériel salifère triasique interstratifié dans l'Albien: Extension du domaine à "glacier de sel" sous-marin des confins algéro-tunisiens. Comptes Rendus de l'Académie des Sciences, **318**, 1661–1667 (in French).

Vila J. M., Ben Youssef M., Chikhaoui M., Ghanmi M., 1996: Un grand "glacier de sel" sous marin albien moyen du Nord-Ouest tunisien (250 Km^2?): Le matériel salifère triasique du "diapir" de Ben Gasseur et de l'anticlinal d'El Kef. Comptes Rendus de l'Académie des Sciences, **322**, 221–227 (in French).

Werner S., 1953: Interpretation of Magnetic Anomalies at Sheet-like Bodies. Sveriges Geologiska Undersokning, Arsbok, **43**, 6.

Wijns C., Perez C., Kowalczyk P., 2005: Theta map: Edge detection in magnetic data. Geophysics, **70**, 39–43.

Zaier A., 1999a: Carte géologique au 1/50000 d'Ain Ksiba. Feuille No 60. Office National des Mines. Tunisie.

Zaier A., 1999b: Evolution tectono-sédimentaire du basin phosphate du centre-ouest de la Tunisie Minéralogie, pétrographie, géochimie et genèse des phosphorites. PhD. Thesis., Université de Tunis II, Faculté des sciences de Tunis (in French).

sciendo

Contributions to Geophysics and Geodesy Vol. 48/2, 2018 (161–178)

Interpretation of gravity anomalies due to simple geometric-shaped structures based on quadratic curve regression

Mohammed TLAS, Jamal ASFAHANI

Atomic Energy Commission, P. O. Box 6091, Damascus, Syria; e-mail: pscientific@aec.org.sy

Abstract: An easy and very simple method to interpret residual gravity anomalies due to simple geometrical shaped models such as a semi-infinite vertical rod, an infinite horizontal rod, and a sphere has been proposed in this paper. The proposed method is mainly based on the quadratic curve regression to best-estimate the model parameters, e.g. the depth from the surface to the center of the buried structure (sphere or infinite horizontal rod) or the depth from the surface to the top of the buried object (semi-infinite vertical rod), the amplitude coefficient, and the horizontal location from residual gravity anomaly profile. The proposed method has been firstly tested on synthetic data set corrupted and contaminated by a Gaussian white noise level to demonstrate the capability and the reliability of the method. The results acquired show that the estimated parameters values derived by this proposed method are very close to the assumed true parameters values. Next, the validity of the presented method is demonstrated on synthetic data set and 3 real data sets from Cuba, Sweden and Iran. A comparable and acceptable agreement is indicated between the results derived by this method and those from the real field data information.

Key words: gravity anomaly, sphere-like structure, semi-infinite vertical rod-like structure, infinite horizontal rod-like structure, quadratic curve regression

1. Introduction

The gravity method is one of the first geophysical techniques used in oil and gas exploration. Most of the geological structures in oil and mineral exploration can be approximated by simple geological structures such as a fault, a sphere, a cylinder, a sheet, semi-infinite vertical rod, an infinite horizontal rod or a dike. According to this approximation, different methods have been already introduced to interpret gravity field anomalies due to simple geometric models in an attempt to best-estimate the gravity

doi: 10.2478/congeo-2018-0006

parameters values, e.g. the depth to the buried body and the amplitude coefficient. Those interpretation methods include, linear optimization-simplex algorithm (*Asfahani and Tlas, 2015*), neural network modeling (*Abedi et al., 2010*), differential evolution algorithm (*Ekinci et al., 2016*), graphical methods (*Nettleton, 1962 and 1976*), ratio methods (*Bowin et al., 1986; Abdelrahman et al., 1989*), Fourier transform (*Odegard and Berg, 1965; Sharma and Geldart, 1968*), Euler deconvolution (*Thompson, 1982*), neural network (*Elawadi et al., 2001*), Mellin transform (*Mohan et al., 1986*), least-squares minimization approaches (*Gupta, 1983; Lines and Treitel, 1984; Abdelrahman, 1990; Abdelrahman et al., 1991; Abdelrahman and El-Araby, 1993; Abdelrahman and Sharafeldin, 1995a*), Werner deconvolution (*Hartman et al., 1971; Jain, 1976*). *Kilty (1983)* extended the Werner deconvolution technique to the analysis of gravity data using both the residual anomaly and its first and second horizontal derivatives, *Ku and Sharp (1983)* further refined the method by using iteration for reducing and eliminating the interference field and then applied Marquardt's non-linear least squares method to further refine automatically the first approximation provided by deconvolution. *Salem and Ravat (2003)* presented a new automatic method for the interpretation of magnetic data, called AN-EUL. Their method is based on a combination of the analytic signal and the Euler deconvolution method. With the AN-EUL, both the location and the approximate geometry of a magnetic source can be deduced. *Fedi (2007)* described the theory for the gravity and magnetic fields and their derivatives for any order, and proposed a method called depth from extreme points (DEXP) to interpret any potential field. The DEXP method allows estimating of source depths, density and structural index from the extreme points of a 3D field scaled according to specific power laws of the altitude. *Salem and Smith (2005)* presented an alternative method to estimate both the depth and model type using the first order local wave number approach without the need for third order derivatives of the field. In their method, a normalization of the first order local wave-number anomalies is achieved, and a generalized equation to estimate the depth of some 2D magnetic sources regardless of the source structure is obtained. *Silva and Barbosa (2003)* derived the analytical estimators for the horizontal and vertical source position in 3D Euler deconvolution as a function of the x, y, and z derivatives of the magnetic anomaly within a data window. *Barbosa et al. (1999)* proposed a new crite-

rion for determining the structural index, based on the correlation between the total magnetic field anomaly and the estimates of an unknown base level. *Salem et al. (2008)* developed a new method for the interpretation of gridded magnetic data, which based on derivatives of the tilt angle, where a simple linear equation, similar to the 3D Euler equation can be obtained. Their method estimates both the horizontal location and the depth of magnetic bodies, but without specifying prior information about the nature of the sources. *Fedi et al. (2009)* proposed a new method based on a 3D multiridge analysis of potential field. The new method assumes a 3D subset in the harmonic region and studies the behavior of the potential field ridges, which are built by joining extreme points of the analyzed field computed at different altitudes.

However, only few techniques have treated the determination of shape of the buried structure. These techniques include, for example, Walsh transform (*Shaw and Agarwal, 1990*), least-squares methods (*Abdelrahman and Sharafeldin, 1995b; Abdelrahman et al., 2001a, b*), constrained and penalized nonlinear optimization technique (*Tlas et al., 2005*). Generally, the determination of the depth, shape factor, and amplitude coefficient of the buried structure is performed by these methods from residual gravity anomaly, where the accuracy of the results, obtained by them, depends on the accuracy in which the residual anomaly can be separated and isolated from the observed gravity anomaly.

Recently, *Asfahani and Tlas (2012)* proposed an efficient approach to interpret the residual gravity anomalies in order to estimate the gravity parameters, e.g. depth, amplitude coefficient and geometric shape factor of simple buried bodies, such as a sphere, horizontal cylinder and vertical cylinder. The method is based on the non-convex and nonlinear Fair function minimization and the adaptive simulated annealing, stochastic optimization algorithm. The main advantage of this approach is that the buried body shape is considered as unknown factor and can be estimated as an independent parameter. However, this approach suffers from the discrepancy and has some disadvantages, because it sometimes necessitates the use of multi-starting or initial guesses of parameters in order to assure the global convergence or to reach the global minima of the objective function.

A recent publication by*Asfahani and Tlas (2015)* focused on a new practical interpretation methodology for interpreting residual gravity field

anomalies and best-estimating of model parameters values, e.g. the depth to the top or to the center of the body and the amplitude coefficient related to a buried sphere or a cylinder-like structure. The method uses the deconvolution technique to avoid the local minima, where the nonlinear optimization problem describing the suitable simple geometric-shaped model of structure is transformed into a linear optimization one. The linear problem is thereafter solved by the very well-known algorithm in linear optimization called the simplex algorithm of Dantzig (*Phillips et al., 1976*) in order to definitely reach the global minima.

In this paper, an easy and simple interpretation method based on quadratic polynomial regression is proposed for interpreting residual gravity field anomalies and for best-estimating of model parameters values, e.g. the depth to the top or to the center of the body, the horizontal location and the amplitude coefficient related to a buried sphere, semi-infinite vertical rod or infinite horizontal rod. The reliability and capability of the proposed interpretation method is demonstrated using synthetic data set and contaminated by a white Gaussian noise level of 25%. The results acquired show that the estimated parameter values derived by this method are very close to the assumed true values of parameters.

The validity of this method is also demonstrated using three real field gravity anomalies taken from Cuba, Sweden and Iran. Comparable and acceptable agreements are shown between the results derived by the proposed method and those obtained by other interpretation methods. Moreover, the depth obtained by such a proposed method is found to be in high accordance with that obtained from the real field data information.

2. Theory

A theoretical and synthetic residual gravity anomaly related to various geological models such as a sphere, a semi-infinite vertical rod and an infinite horizontal rod have been treated in this research, in order to demonstrate the validity and the applicability of the proposed interpretation method.

The general expression of the residual gravity anomaly (V) at any point $M(x)$ along the x-axis of a semi-infinite vertical rod-like structure, an infinite horizontal rod-like structure and a sphere-like structure, in a Carte-

sian coordinate system (Fig. 1) can be given according to *Nettleton (1962), Gupta (1983)* as:

$$V_z(x_i) = \frac{k}{\left((x_i - x_0)^2 + z^2\right)^q} \quad (i = 1, ..., N), \tag{1}$$

where q is the geometrical shape factor of the buried structure given as: $q = 1.5$ for a sphere, $q = 0.5$ for a semi-infinite vertical rod and $q = 1$ for an infinite horizontal rod, x_0 is the horizontal location of the buried body, z is the depth from the surface to the center of the buried structure (sphere or infinite horizontal rod) or the depth from the surface to the top of the buried object (semi-infinite vertical rod), k is the amplitude coefficient

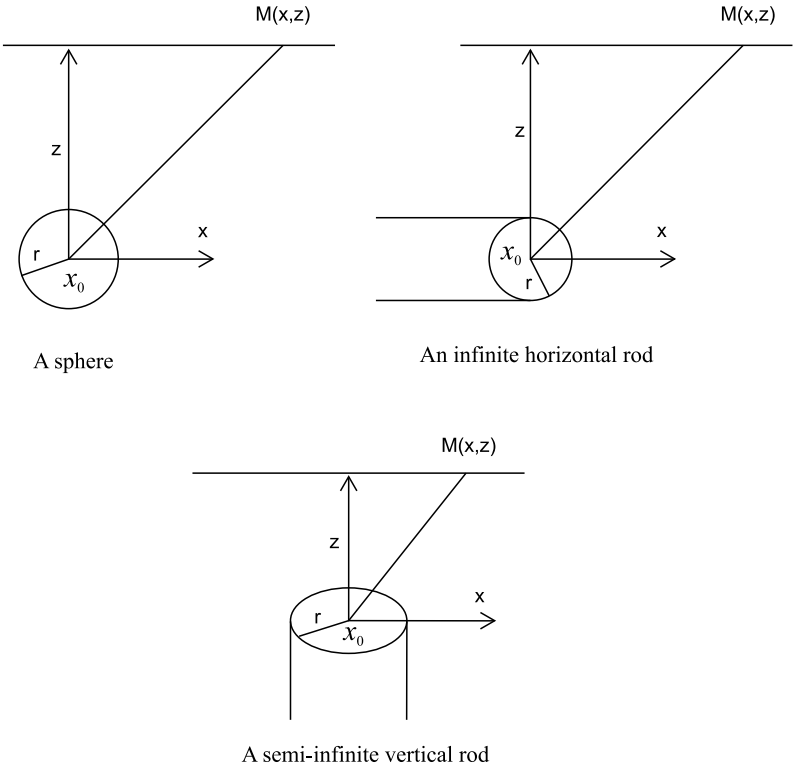

Fig. 1. Diagrams of simple geometrical structures (sphere, semi-infinite vertical rod and infinite horizontal rod).

given by: $k = \frac{4}{3}\pi G\rho r^3 z$ for a sphere, $k = \pi G\rho r^2$ for a semi-infinite vertical rod and $k = 2\pi G\rho r^2 z$ for an infinite horizontal rod, where ρ is the density contrast, G is the universal gravitational constant, r is the radius, and finally x_i $(i = 1, \ldots, N)$ is the horizontal position coordinate.

The set of Eq. (1) consists of N nonlinear equations in function of the three independent parameters k, x_0 and z. The term V_i will be used, for simplification, instead of the term $V_z(x_i) \quad (i = 1, ..., N)$, in the rest of the paper.

From Eq. (1), it can be easily observed that the sign of the parameter k is similar and coincident to the sign of $V_i\,(i = 1, ..., N)$.

Taking the absolute values of both sides of Eq. (1) we find

$$|V_i| = \frac{|k|}{\left((x_i - x_0)^2 + z^2\right)^q} \quad (i = 1, ..., N). \tag{2}$$

The simple manipulation of the Eq. (2) will give us

$$|V_i|^{-\frac{1}{q}} = |k|^{-\frac{1}{q}} x_i^2 - 2x_0|k|^{-\frac{1}{q}} x_i + |k|^{-\frac{1}{q}} \left(x_0^2 + z^2\right) \quad (i = 1, ..., N). \tag{3}$$

And with help of the following symbolism:

$$A = |k|^{-\frac{1}{q}}, \tag{4}$$

$$B = -2x_0|k|^{-\frac{1}{q}}, \tag{5}$$

$$C = |k|^{-\frac{1}{q}} \left(x_0^2 + z^2\right). \tag{6}$$

The Eq. (3) can be written as

$$|V_i|^{-\frac{1}{q}} = Ax_i^2 + Bx_i + C \quad (i = 1, ..., N). \tag{7}$$

The right hand side in Eq. (7), is a quadratic polynomial in function of x_i, the values of the coefficients A, B, and C, can be determined through performing a quadratic curve regression between x_i and $y_i = |V_i|^{-\frac{1}{q}} \quad (i = 1, ..., N)$ using one of the familiar statistical programs as Microsoft Excel or through solving the following set of simultaneously linear equations by the well-known direct method of Gauss

$$\left.\begin{aligned}
\left(\sum_{i=1}^{N} x_i^4\right) A + \left(\sum_{i=1}^{N} x_i^3\right) B + \left(\sum_{i=1}^{N} x_i^2\right) C &= \sum_{i=1}^{N} x_i^2 |V_i|^{-\frac{1}{q}} \\
\left(\sum_{i=1}^{N} x_i^3\right) A + \left(\sum_{i=1}^{N} x_i^2\right) B + \left(\sum_{i=1}^{N} x_i\right) C &= \sum_{i=1}^{N} x_i |V_i|^{-\frac{1}{q}} \\
\left(\sum_{i=1}^{N} x_i^2\right) A + \left(\sum_{i=1}^{N} x_i\right) B + NC &= \sum_{i=1}^{N} |V_i|^{-\frac{1}{q}}
\end{aligned}\right\} . \tag{8}$$

After knowing the unique optimal values of A, B, and C, then the best-estimate of the amplitude coefficient (k) can be easily obtained from Eq. (4) as:

$$k = \frac{1}{A^q} , \text{ when } V_i \geq 0 \ (i = 1, ..., N), \tag{9}$$

$$k = -\frac{1}{A^q} , \text{ when } V_i \leq 0 \ (i = 1, ..., N). \tag{10}$$

Also, the best-estimate of the horizontal location (x_0) of the buried body can be found from Eq. (5) as:

$$x_0 = -\frac{B}{2A} . \tag{11}$$

Finally, the best- estimate of the depth (z) from the surface to the center of the buried structure (sphere or infinite horizontal rod) or the depth from the surface to the top of the buried object (semi-infinite vertical rod) can be reached from Eq. (6) as:

$$z = \frac{\sqrt{|4AC - B^2\ |}}{2A} . \tag{12}$$

It is useful to mention that there is no loss of generality in assuming the source geometry of the gravity anomaly is a priori known. There are in addition no imposed restrictions on the generality of the proposed interpretation method.

Before explaining how we can solve this ambiguity and this inconvenience, we will define the statistical criterion of preference called the Root Mean Square Error (*RMSE; Collins, 2003*), based on the minimal value, between the field gravity data anomaly and the computed gravity one, using

the estimated values of z, x_0 and k resulted from Eqs. (9–12) for a specific value of the geometric shape factor $q = 0.5, 1$, and 1.5. The formula of this statistical criterion is given as:

$$RMSE = \sqrt{\frac{\sum_{i=1}^{N} \left(V_i^O - V_i^C\right)^2}{N}}, \tag{13}$$

where V_i^O and V_i^C $(i = 1, ..., N)$ are the observed and the computed gravity values at the point x_i $(i = 1, ..., N)$, respectively.

In the case where the source geometry of the gravity field anomaly is unknown, the following next procedure composed of three steps should be followed:

First, the gravity field anomaly is interpreted by adapting and assuming the source geometry as a semi-infinite vertical rod ($q = 0.5$), where Root Mean Square Error $RMSE\_V$ is computed using Eq. (13) with the estimated values of z, x_0 and k derived from Eqs. (9–12).

Second, the gravity field anomaly is re-interpreted by adapting the source geometry as an infinite horizontal rod ($q = 1$), where the Root Mean Square Error $RMSE\_H$ is also computed using Eq. (13) with the estimated values of z, x_0 and k derived from Eqs. (9–12).

Third, the gravity field anomaly is re-interpreted by assuming the source geometry as a sphere ($q = 1.5$), where the Root Mean Square Error $RMSE\_S$ is also computed using Eq. (13) with the estimated values of z, x_0 and k derived from Eqs. (9–12).

The lowest one of the three reached values of $RMSE\_V$, $RMSE\_H$ and $RMSE\_S$ is selected as a convincible solution, which exactly indicates to the suitable source geometry related to the responsible gravity field anomaly.

The square of correlation coefficient is another statistical criterion of preference that can be also applied to select the best optimum gravity solution. It is defined through the following mathematical expression:

$$R^2 = \frac{\left(\sum_{i=1}^{N} \left(V_i^O - \bar{V}^O\right) \times \left(V_i^C - \bar{V}^C\right)\right)^2}{\sum_{i=1}^{N} \left(V_i^O - \bar{V}^O\right)^2 \times \sum_{i=1}^{N} \left(V_i^C - \bar{V}^C\right)^2}, \tag{14}$$

where $\bar{V}^O$ and $\bar{V}^C$ are the arithmetic means of V_i^O and V_i^C $(i = 1, ..., N)$

respectively. We calculate R-squared for the three assumed types of geometric shapes of the buried structure, R^2_V, R^2_H and R^2_S for a semi-infinite vertical rod ($q = 0.5$), an infinite horizontal rod ($q = 1$), and a sphere ($q = 1.5$) respectively, by using Eq. (14) with the estimated values of z, x_0 and k resulted from Eqs. (9–12).

The highest one of the three reached values of R^2_V, R^2_H and R^2_S is selected as a convincible solution, which exactly and in directly indicates to the suitable source geometry related to the responsible gravity field anomaly.

3. Test on the synthetic data

A synthetic gravity anomaly $V_z(x_i)$ $(i = 1, ..., N)$ due to a spherical structure is generated from Eq. (1), by using the following values of model parameters: geometric shape factor $q = 1.5$, depth from the surface to the center of the buried spherical structure $z = 35\,\mathrm{m}$, amplitude coefficient $k = 1500\,\mathrm{mGal\,m^3}$ and the horizontal location $x_0 = 5\,\mathrm{m}$.

The generated synthetic anomaly is perturbed and contaminated by a Gaussian random noise of 25% maximum, using continuous normal distribution, where one additional gravity anomaly is generated (Fig. 2). This regenerated gravity anomaly is consequently interpreted by the proposed method. Table 1 summarizes all acquired results concerning this anomaly, the geophysical parameters (z, k, x_0) and the preference criterions $(RMSE, R^2)$, and this for the three structures a priori assumed; a semi-infinite vertical rod, an infinite horizontal rod and a sphere.

Table 1 shows that the lowest $RMSE$ of the three reached values of $RMSE\_V$, $RMSE\_H$ and $RMSE\_S$ or the highest one of the three reached values of R^2_V, R^2_H and R^2_S, and clearly indicates that the suitable source geometry related to the responsible contaminated synthetic gravity anomaly is a sphere.

The results documented and presented in Table 1 show without any doubt that the estimated parameter values, derived by the proposed interpretation method, are very close to the true assumed values of parameters. This clearly proves the efficiency and the capability of the new proposed interpretation method.

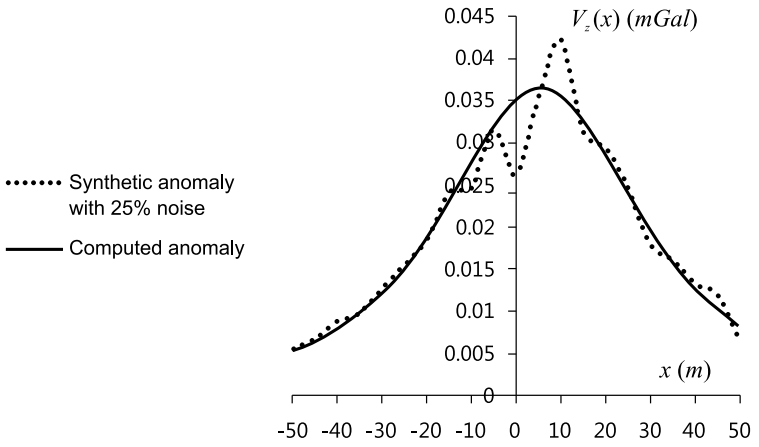

Fig. 2. The effect of the sphere without the noise (solid line) and with 25% noise added (dotted line). The model parameters are in the Table 1.

Table 1. Interpretation of a synthetic gravity anomaly with 25% maximum level of Gaussian random noise.

Source geometric shape	Model parameters	True values of model parameters	Estimated values of model parameters with maximum 25% random noise
Semi-infinite vertical rod ($q = 0.5$)	z (m)	35	13.60
	k (mGal m) x_0 (m)	1500 5	0.33 5.54
	$RMSE$ (mGal) R^2	– –	0.0083 0.9102
Infinite horizontal rod ($q = 1$)	z (m)	35	22.03
	k (mGal m^2) x_0 (m)	1500 5	20.25 4.97
	$RMSE$ (mGal) R^2	– –	0.0037 0.9155
Sphere ($q = 1.5$)	z (m)	35	34.83
	k (mGal m^3) x_0 (m)	1500 5	1503.20 4.76
	$RMSE$ (mGal) R^2	– –	0.0027 0.9276

4. Tests on the real data

Three field residual gravity anomalies over various geological structures are interpreted by the new proposed method. The three field gravity anomalies are interpreted according to the three different geological structures, e.g. a sphere, an infinite horizontal rod, and a semi-infinite vertical rod. The resulting model with the lowest reached value of $RMSE$ or the highest reached value of R^2 is selected as the best and the suitable model for estimating the parameters of the field residual gravity anomaly.

4.1. Chromites deposit residual field gravity anomaly, Cuba

Fig. 3 shows a normalized residual field gravity anomaly measured over a chromites deposit in Camaguey province, Cuba (*Robinson and Coruh, 1988*). The gravity anomaly has been interpreted by the proposed method assuming a priori the source geometry is a semi-infinite vertical rod ($q = 0.5$), an infinite horizontal rod ($q = 1$), and sphere ($q = 1.5$). Table 2 shows in details all the obtained results related to this anomaly.

From Table 2, the lowest $RMSE$ of the three reached values of $RMSE\_V$, $RMSE\_H$ and $RMSE\_S$ or the highest one of the three reached values of

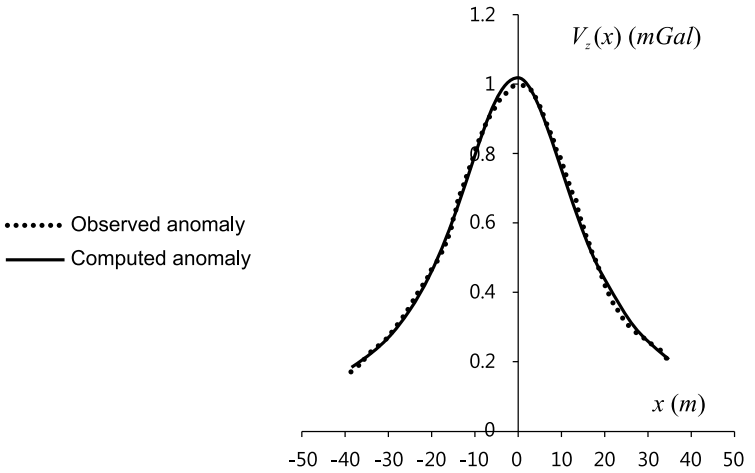

Fig. 3. Normalized residual gravity field anomaly over a chromites deposit, Camaguey province, Cuba (dotted line). The evaluated curve by the proposed method is presented for an infinite horizontal rod model (solid line). The model parameters are in the Table 2.

Table 2. Interpretation of the Chromites field residual gravity anomaly, Cuba.

Model parameters	Semi-infinite vertical rod	Infinite horizontal rod	Sphere
z (m)	7.94	17.55	26.50
k	7.24 (mGal m)	318.55 (mGal m^2)	17256.00 (mGal m^3)
x_0 (m)	0.22	–0.44	–0.62
$RMSE$ (mGal)	0.1264	0.0170	0.0351
R^2	0.9526	0.9969	0.9923

R^2_V, R^2_H and R^2_S has been obtained for the infinite horizontal rod. Results of $RMSE$ and R^2 mean that the field residual gravity anomaly is must to be preferably modeled as an infinite horizontal rod.

The depth obtained in this case ($z = 17.55$ m) is found to be in a good agreement with that obtained from drill-hole information ($z = 21$ m). The computed gravity anomaly has been drawn according to these estimated values of infinite horizontal rod model parameters as shown in Fig. 3. The comparison between field and computed anomalies clearly indicates the close agreement between them, which attests the capability and the validity of the proposed method.

4.2. Karrbo residual field gravity anomaly, Sweden

Fig. 4 shows a field residual gravity anomaly of a profile 25.6 m length measured over the two-dimensional pyrrhotite ore, Karrbo, Vastmanland, Sweden (*Shaw and Agarwal, 1990*). The field gravity anomaly has been also interpreted by the proposed method for the three different geological structures a priori assumed. Table 3 shows the complete obtained results related to this interpreted anomaly.

From Table 3, the lowest $RMSE$ of the three reached values of $RMSE\_V$, $RMSE\_H$ and $RMSE\_S$ or the highest one of the three reached values of R^2_V, R^2_H and R^2_S has been obtained for the infinite horizontal rod, meaning that, the field residual gravity anomaly is preferably to be modeled as an infinite horizontal rod.

The depth in this case ($z = 4.69$ m) is found to be in good agreement with the depth reported by *Tlas et al. (2005)* ($z = 4.82$ m), *Asfahani and Tlas (2015)* ($z = 4.7$ m), *Shaw and Agarwal (1990)* ($z = 5.8$ m), and *El-Araby (2000)* ($z = 5.23$ m). The computed gravity anomaly has been drawn

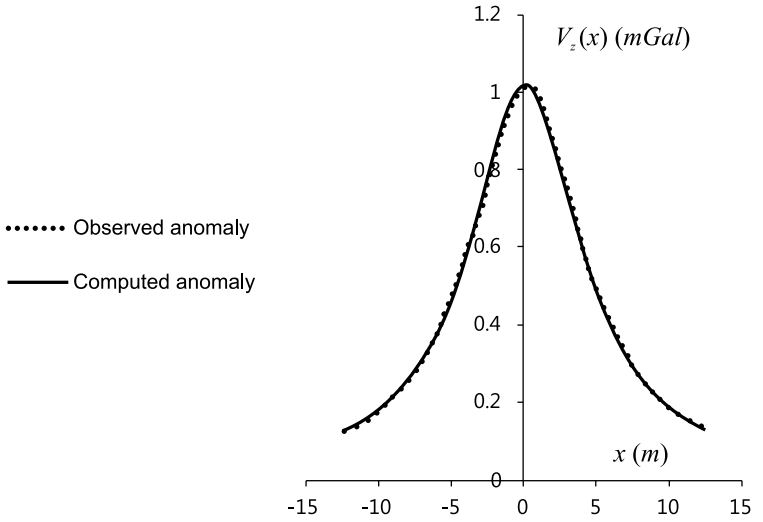

Fig. 4. Residual gravity field anomaly over the two-dimensional pyrrhotite ore, Karrbo, Vastmanland, Sweden (dotted line). The evaluated curve by the proposed method is presented for an infinite horizontal rod model (solid line). The model parameters are in the Table 3.

Table 3. Interpretation of the Karrbo field residual gravity anomaly, Sweden.

Model parameters	Semi-infinite vertical rod	Infinite horizontal rod	Sphere
z (m)	3.04	4.69	7.50
k	1.67 (mGal m)	22.45 (mGal m^2)	365.95 (mGal m^3)
x_0 (m)	0.27	0.21	0.19
$RMSE$ (mGal)	0.2381	0.0063	0.0530
R^2	0.9971	0.9996	0.9869

according to these estimated values of infinite horizontal rod model parameters as shown in Fig. 4. The comparison between field and computed anomalies clearly indicates the close agreement between them, which attests the capability and the validity of the suggested method.

4.3. Dehloran residual field gravity anomaly, Iran

Fig. 5 shows a field residual gravity anomaly measured over an area located in West of Iran in the Zagros tectonic zone, Iran (*Abedi et al., 2010*). The

field gravity anomaly has been also interpreted by the proposed method; the obtained results for this anomaly are completely summarized in Table 4.

From Table 4, the lowest one of the three reached values of $RMSE\_V$, $RMSE\_H$ and $RMSE\_S$ or the highest one of the three reached values of R^2_V, R^2_H and R^2_S has been obtained for the infinite horizontal rod, meaning that, the field residual gravity anomaly is preferably to be modeled as an infinite horizontal rod.

The depth obtained in this case ($z = 24.59$ m) is found to be in good agreement with that reported by (*Abedi et al., 2010*) by using three different interpretation methods, the normalized method ($z = 23.73$ m), the least-

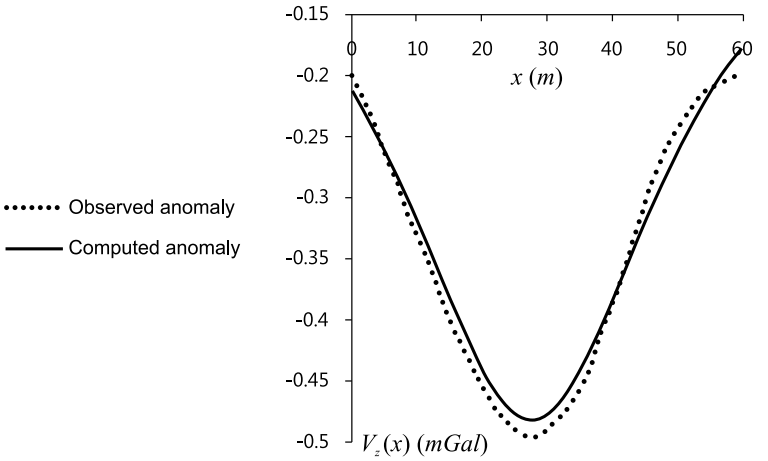

Fig. 5. Residual gravity field anomaly over an area located in West of Iran in the Zagros tectonic zone, Iran (dotted line). The evaluated curve by the proposed method is presented for an infinite horizontal rod model (solid line). The model parameters are in the Table 4.

Table 4. Interpretation of the Dehloran field residual gravity anomaly, Iran.

Model parameters	Semi-infinite vertical rod	Infinite horizontal rod	Sphere
z (m)	12.26	24.59	32.74
k	–6.52 (mGal m)	–291.46 (mGal m^2)	–16641.00 (mGal m^3)
x_0 (m)	27.42	27.62	27.69
$RMSE$ (mGal)	0.0171	0.0129	0.0158
R^2	0.9785	0.9892	0.9834

squares method ($z = 23.31$ m), the neural network method ($z = 22.8$ m) and also with that obtained from drill-hole information ($z = 23$ m).

The computed gravity anomaly has been drawn according to these estimated values of infinite horizontal rod model parameters as shown in Fig. 5. The comparison between field and computed anomalies clearly indicates the close agreement between them, which attests the capability and the validity of the suggested method.

5. Conclusion

A new simple and very easy method is proposed herein for the interpretation of residual gravity anomalies due to different simple geometric-shaped models such as a semi-infinite vertical rod, an infinite horizontal rod and a sphere. The proposed interpretative method is mainly based on quadratic curve fitting to best-estimate the model parameters values, e.g. the depth to the top or to the center of the buried structure, the amplitude coefficient and the horizontal location from a residual gravity anomaly profile. The method has been firstly tested on synthetic data set corrupted and contaminated by a white Gaussian random noise maximum level of 25% in order to demonstrate its reliability and its capability. The results acquired show clearly that the estimated parameter values derived by the proposed method are very close to the assumed true values of parameters.

The validity and the applicability of this new method are also demonstrated by applying it to three real field gravity anomalies from Cuba, Sweden and Iran. A comparable and acceptable agreement is shown between the results derived by the method and those obtained by other interpretation methods.

Moreover, the depth obtained by such a proposed method is found to be in high accordance with that obtained from the real field data information.

The interpretation method can be easily put in MATLAB code or in Excel sheet. Therefore, the new proposed methodology of interpretation is highly recommended for routine analysis of gravity anomalies in an attempt to determine the best-estimate values of parameters related to spheres, semi-infinite vertical rods and infinite horizontal rods-like structures.

Acknowledgements. Authors would like to thank Dr. I. Othman Director General of the Syrian Atomic Energy Commission for his continuous encouragement and guidance to achieve this research. Also, authors would like to deeply thank the two anonymous reviewers for their considerable contribution that improved the revised version and Dr. Igor Kohut, Editor of Contribution to Geophysics and Geodesy for his collaboration with us during the different processes of this paper.

References

Abdelrahman E. M., El-Araby T. M., El-Araby H. M, Abo-Ezz E. R., 2001a: Three least-squares minimization approaches to depth, shape, and amplitude coefficient determination from gravity data. Geophysics, **66**, 1105–1109.

Abdelrahman E. M., El-Araby T. M., El-Araby H. M, Abo-Ezz E. R., 2001b: A new method for shape and depth determinations from gravity data. Geophysics, **66**, 1774–1780.

Abdelrahman E. M., Sharafeldin S. M., 1995a: A least-squares minimization approach to depth determination from numerical horizontal gravity gradients. Geophysics, **60**, 1259–1260.

Abdelrahman E. M., Sharafeldin S. M., 1995b: A least-squares minimization approach to shape determination from gravity data. Geophysics, **60**, 589–590.

Abdelrahman E. M., El-Araby T. M., 1993: A least-squares minimization approach to depth determination from moving average residual gravity anomalies. Geophysics, **59**, 1779–1784.

Abdelrahman E. M., Bayoumi A. I., El-Araby H. M., 1991: A least-squares minimization approach to invert gravity data. Geophysics, **56**, 115–118.

Abdelrahman E. M., 1990: Discussion on "A least-squares approach to depth determination from gravity data" by Gupta O. P., Geophysics, **55**, 3, 376–378.

Abdelrahman E. M., Bayoumi A. I., Abdelhady Y. E., Gobash M. M., El-Araby H. M., 1989: Gravity interpretation using correlation factors between successive least-squares residual anomalies. Geophysics, **54**, 12, 1614–1621.

Abedi M., Afshar A., Ardestani V. E., Norouzi G. H., Lucas C., 2010: Application of various methods for 2D inverse modeling of residual gravity anomalies. Acta Geophysica, **58**, 2, 317–336.

Asfahani J., Tlas M., 2012: Fair function minimization for direct interpretation of residual gravity anomaly profiles due to spheres and cylinders. Pure and Applied Geophysics, **169**, 157–165.

Asfahani J., Tlas M., 2015: Estimation of gravity parameters related to simple geometrical structures by developing an approach based on deconvolution and linear optimaization techniques. Pure and Applied Geophysics, **172**, 10, 2891–2899.

Barbosa V. C. F., Silva J. B. C., Medeiros W. E., 1999: Stability analysis and improvement of structural index estimation in Euler deconvolution. Geophysics, **64**, 1, 48–60.

Bowin C., Scheer E., Smith W., 1986: Depth estimates from ratios of gravity, geoid and gravity gradient anomalies. Geophysics, **51**, 123–136.

Collins G. W., 2003: Fundamental numerical methods and data analysis, Case Western Reserve University.

Ekinci Y. L., Balkaya Ç., Göktürkler G., Turan S., 2016: Model parameter estimations from residual gravity anomalies due to simple-shaped sources using Differential Evolution Algorithm. Journal of Applied Geophysics, **129**, 133–147.

El-Araby H. M., 2000: An iterative least-squares minimization approach to depth determination from gravity anomalies. Bull Fac Sci, Cairo Univ, **68**, 233–243.

Elawadi E., Salem A., Ushijima K., 2001: Detection of cavities from gravity data using a neural network. Exploration Geophysics, **32**, 75–79.

Fedi M., 2007: DEXP: A fast method to determine the depth and the structural index of potential fields sources. Geophysics, **72**, 1, I1–I11.

Fedi M., Florio G., Quarta T. A. M., 2009: Multiridge analysis of potential fields: Geometric method and reduced Euler deconvolution. Geophysics, **74**, 4, L53–L65.

Gupta O. P., 1983: A least-squares approach to depth determination from gravity data. Geophysics, **48**, 360–375.

Hartmann R. R., Teskey D., Friedberg I., 1971: A system for rapid digital aeromagnetic interpretation. Geophysics, **36**, 891–918.

Jain S., 1976: An automatic method of direct interpretation of magnetic profiles. Geophysics, **41**, 531–541.

Kilty T. K., 1983: Werner deconvolution of profile potential field data. Geophysics, **48**, 234–237.

Ku C. C., Sharp J. A., 1983: Werner deconvolution for automatic magnetic interpretation and its refinement using Marquardt's inverse modeling. Geophysics, **48**, 754–774.

Lines L. R., Treitel S., 1984: A review of least-squares inversion and its application to geophysical problems. Geophysical Prospecting, **32**, 159–186.

Mohan N. L., Anandababu L., Roa S., 1986: Gravity interpretation using the Melin transform. Geophysics, **51**, 114–122.

Nettleton L. L., 1962: Gravity and magnetics for geologists and seismologists. AAPG, **46**, 1815–1838.

Nettleton L. L., 1976: Gravity and magnetic in oil prospecting: Mc-Graw Hill Book Co.

Odegard M. E., Berg J. W., 1965: Gravity interpretation using the Fourier integral. Geophysics, **30**, 424–438.

Phillips D. T., Ravindra A., Solber J. J., 1976: Operations research. John Wiley and Sons, Inc.

Robinson E. S., Coruh C., 1988: Basic exploration geophysics. Wiley, New York, NY, 562 pp.

Salem A., Ravat D., 2003: A combined analytic signal and Euler method (AN-EUL) for automatic interpretation of magnetic data. Geophysics, **68**, 6, 1952–1961.

Salem A., Smith R., 2005: Depth and structural index from normalized local wavenumber of 2D magnetic anomalies. Geophysical Prospecting, **53**, 83–89.

Salem A., Williams S., Fairhead D., Smith R., Ravat D., 2008: Interpretation of magnetic data using tilt angle derivatives. Geophysics, **73**, 1.

Sharma B., Geldart L. P., 1968: Analysis of gravity anomalies of two-dimensional faults using Fourier transforms. Geophysical prospecting, **16**, 77–93.

Shaw R. K., Agarwal S. N. P., 1990: The application of Walsh transform to interpret gravity anomalies due to some simple geometrically shaped causative sources: A feasibility study. Geophysics, **55**, 843–850.

Silva J. B. C., Barbosa V. C. F., 2003: 3D Euler deconvolution: Theoretical basis for automatically selecting good solution. Geophysics, **68**, 6, 1962–1968.

Thompson D. T., 1982: EULDPH-a new technique for making computer-assisted depth estimates from magnetic data. Geophysics, **47**, 31–37.

Tlas M., Asfahani J., Karmeh H., 2005: A versatile nonlinear inversion to interpret gravity anomaly caused by a simple geometrical structure. Pure and Applied Geophysics, **162**, 2557–2571.

sciendo

Contributions to Geophysics and Geodesy Vol. 48/2, 2018 (179–190)

The refined Moho depth map in the Carpathian-Pannonian region

Miroslav BIELIK[1,3], Irina MAKARENKO[2], Kristián CSICSAY[3], Olga LEGOSTAEVA[2], Vitaly STAROSTENKO[2], Aleksandra SAVCHENKO[2], Barbora ŠIMONOVÁ[1], Jana DÉREROVÁ[3], Lucia FOJTÍKOVÁ[3], Roman PAŠTEKA[1], Jozef VOZÁR[3]

[1] Department of Applied and Environmental Geophysics, Faculty of Natural Sciences, Comenius University, Mlynská dolina, Ilkovičova 6, 842 48 Bratislava, Slovak Republic; e-mail: bielik@fns.uniba.sk

[2] Institute of Geophysics, National Academy of Sciences of Ukraine, Palladin av. 32, 03680 Kiev, Ukraine

[3] Earth Science Institute, Slovak Academy of Sciences, Dúbravská cesta 9, P. O. Box 106, 840 05 Bratislava, Slovak Republic; e-mail: geofmiro@savba.sk

Abstract: We present a new digital Moho depth map of the Carpathian-Pannonian region. The map was produced by compiling Moho discontinuity depth data, which were obtained by interpretation of seismic measurements taking into account the results of 2-D and 3-D integrated geophysical modelling. The resultant map is characterized by significant Moho-depth variations. The trends and features of the Moho in this region were correlated with tectonic units.

Key words: geophysical interpretation, seismics, Moho depth, Carpathian-Pannonian crust

1. Introduction

Research on the morphology of the Moho boundary (the crustal thickness) in the Carpathian-Pannonian region has a long history. It has been a subject of extensive studies since the 1950s, using the two standard geophysical methods for the determination of the depth to the Moho: seismic reflection and refraction measurements (*Szafián and Horváth, 2006*). The first results of the 2-D and 3-D seismic measurements in the states that fall into the area under investigation were published, for example, in works of

Mayerová et al. (1985, 1994), Bucha and Blížkovský (1994), Guterch et al. (1976, 1983, 1984), Gálfi and Stegena (1960), Szénás (1972), Lazarescu et al. (1983), Dragaševič (1987), Aljinovič (1987), Aric and Gutdeutsch (1987), Sollogub et al. (1973), Sollogub (1988), Chekunov et al. (1988), Kharitonov et al. (1993), Posgay et al. (1996) and *Il'chenko and Buharev (2001).*

To the first works that attempted to compile Moho depth maps belong the publications of *Szénás (1972), Beránek and Zátopek (1981a,b), Guterch et al. (1984, 1986), Šefara et al. (1987), Sollogub (1986), Posgay et al. (1991, 1995), Horváth (1993), Horváth et al. (2006), Dimitrijevič (1995), Lenkey et al. (1998)* and *Lenkey (1999).*

For specific areas of Europe the maps of the depth to Moho were summarized for example in the papers of *Hauser et al., (2001, 2007), Knapp et al. (2005)* and *Martin et al. (2006).*

The results of seismic international projects of the CELEBRATION 2000, ALP 2002 and SUDETES 2003 have contributed exceptional cognition about the crustal thickness in the area of Central Europe. The courses of the Moho interface along the profiles were published in the papers of *Grad et al. (2006, 2009a), Środa et al. (2006), Hrubcová et al. (2005, 2008, 2010), Behm et al. (2007), Brückl et al. (2007, 2010), Hrubcová and Środa (2015), Brückl (2011), Janík et al. (2009, 2011)* and *Malinowski et al. (2009, 2013).*

The digital crustal models of the Moho depth in very small scales were also presented. *Ziegler and Dezes (2006)* produced the Moho depth map for the Western and Central Europe; *Tesauro et al. (2008)* for Europe; *Grad et al. (2009b), Molinari and Morelli (2011)* for European plate; *Artemieva and Thybo (2013)* for Europe, Greenland, and the North Atlantic region.

For completeness, it should be noted that in the past (e.g. *Szafián et al., 1997; Zeyen et al., 2002; Dérerová et al., 2006; Kaban et al., 2010*), as well as in the recent past (e.g. *Alasonati Tašárová et al., 2016; Grinč et al., 2013; Kiss et al., 2015*), the Moho depth calculations have also been made by integrated modelling of the potential fields.

Based on an analysis of the results of the Moho depth determination, we found that in recent years several new Moho depth maps have been published (e.g. *Tesauro et al., 2008; Grad et al., 2009b; Artemieva and Thybo, 2013*), but at too small scales that occupy very large territories. Such maps often miss a more detailed Moho morphology, which has significant impact

on the quality and accuracy of potential field modelling. Therefore, the goal of this paper is to present a new digital model of the Moho depth in a larger scale solely for the Carpathian-Pannonian region and its nearest surrounding tectonic units. In addition, we correlate the regional variations in crustal thickness with the main tectonic units.

2. New model of the crustal thickness

Our compilation is based on digitization of original seismic profiles that were produced in the last 15–20 years. In the area of Ukraine, some data were also older, since there were no newer seismic measurements performed, except for the results along the seismic profile PANCAKE (*Starostenko et al., 2013*). For the new Moho depth model (Fig. 1), the results obtained along

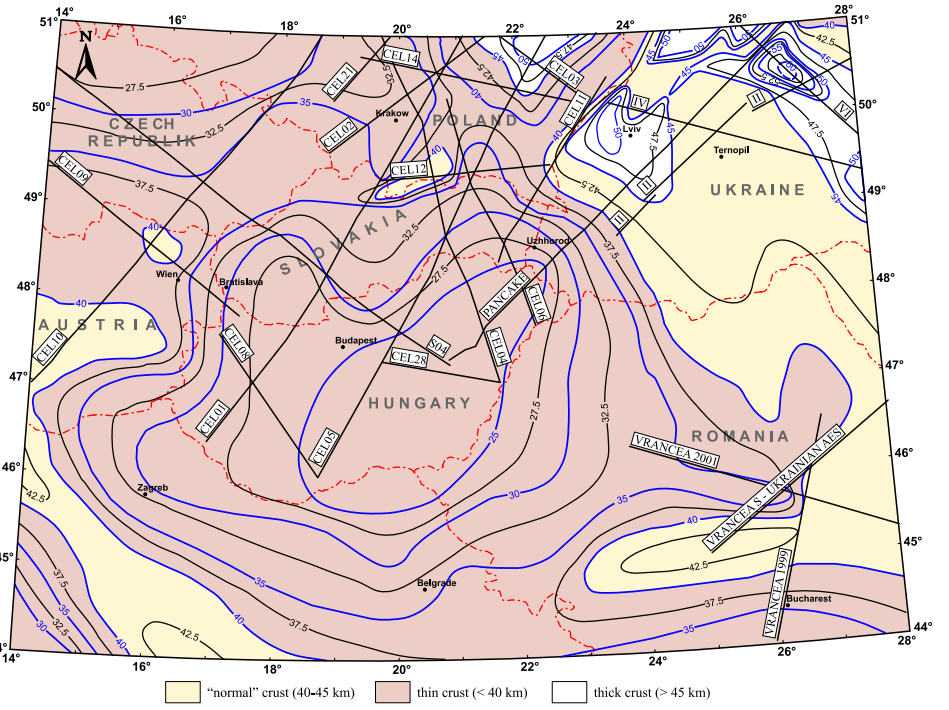

Fig. 1. The Moho depth map in the Carpathian-Pannonian region.

the seismic profiles, which are shown in Table 1, were prominent. There are basically no seismic data for other orogens of the southern Europe (e.g. the Balkanides and the Dinarides, *Artemieva and Thybo, 2013*). From this point of view we used in the Dinarides and Adriatic Sea the results published by *Horváth et al. (2006), Artemieva and Thybo (2013).* For correlation of the Moho depth model with the main tectonic units the tectonic map of the Carpathian-Pannonian region and their surrounding areas is shown in Fig. 2.

Table 1. The profiles that served as key inputs for constructing the Moho depth map.

Profile	**Key references**
CEL01	Środa et al. (2006), Janík et al. (2011)
CEL02	Malinowski et al. (2005), Janík et al. (2009)
CEL03	Janík et al. (2009)
CEL04	Środa et al. (2006), Janík et al. (2011)
CEL05	Grad et al. (2006), Janík et al. (2011)
CEL06	Janík et al. (2011)
CEL08	Malinowski et al. (2003)
CEL09	Hrubcová et al. (2005)
CEL10/Alp04	Hrubcová et al. (2005, 2008), Grad et al. (2009a)
CEL11	Janík et al. (2011)
CEL12	Janík et al. (2011)
CEL14	Janík et al. (2009)
CEL21	Janík et al. (2009)
CEL28	Janík et al. (2011)
VRANCEA99	Hauser et al. (2001)
VRANCEA S - UKRAINIAN AES	Kharitonov et al. (1993)
VRANCEA 2001	Hauser et al. (2007)
PANCAKE	Starostenko et al. 2013
II	Sollogub et al. (1973), Chekunov et al. (1988), Il'chenko and Buharev (2001)
IV	Sollogub (1988)
VI	Sollogub (1988)
SO4	Hrubcová et al. (2010)

3. Correlation of tectonic units with Moho depth

The most interesting feature of the Moho depth map (Fig. 1) is an extraordinarily thin crust, reaching only 24–25 km in its central part of the

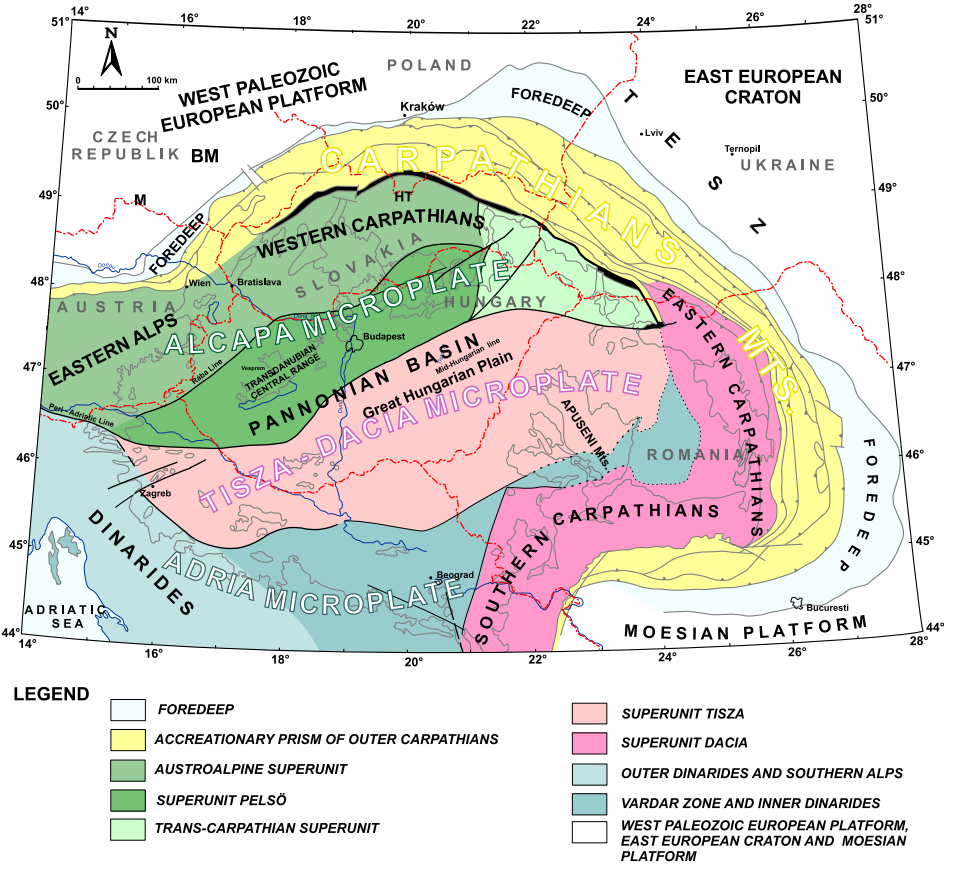

Fig. 2. Tectonic map of the Carpathian-Pannonian basin region (modified after *Bielik 1998 and Kováč, 2000*). BM – Bohemian Massif, M – Moldanubicum, HT – High Tatras, TESZ – Trans European Suture Zone.

Pannonian Basin (the Great Hungarian Plain). From this area, it can be seen that the depth of Moho increases towards all sides. In other words, it grows in the direction to the orogenic regions of the Western, Eastern and Southern Carpathians, Dinarides, Eastern Alps and the Bohemian Massif. The Moho decrease can be observed up to the East European Craton region, where the crust reaches the largest thickness. Here we can see three expressive crustal roots (depressions). The first one is located NE of Krakow and reaches 50 km, while the other (NE of Ternopil') is even larger and is elon-

gated in the NW-SE direction. The crustal thickness reaches ∼60 km, which is the thickest crust in the whole studied area. Both these depressions are split by a third depression, which is characterized by two maximum crustal thicknesses of ∼50 km. Its shape is significantly elongated in the direction of NE–SW. The Trans-European Suture Zone (TESZ) is represented by a linear horizontal gradient of the Moho depth isolines, whose NW–SE direction is identical with the course of this zone. It is interesting to note that the Carpathian Mts. are located over the maximum dip of the Moho in the direction from the Pannonian Basin to the West Paleozoic European platform, the East European Craton and the Moesian Platform. The largest local Moho depression (42 km) in the Western Carpathians is located NE of the High Tatras in Poland. The Bohemian Massif's crust varies from ∼27 km on its NW border to 40 km on its southern one, where it is built by the Moldanubicum. In the Eastern Alps, the thickness of the crust is about 40 km. However, it is well known (*Ziegler and Dezes, 2006*) that this territory is the easiest part of the significant Alpine crustal root (∼55 km). The Dinarides are also characterized by the thicker crust (∼40 km). In the direction to the Adriatic Sea, the crustal thickness thins significantly to only about 30 km.

4. Conclusion

From the resultant Moho depth map the studied area, which is represented by thin (< 40 km), "normal" (40–45 km) and thick (> 45 km) crust, can be divided into the following areas: (a) the Carpathian arc, (b) the Pannonian Basin, (c) the East European Craton, (d) the West Paleozoic European Platform (including the Bohemian Massif), (e) the Trans European Suture Zone, (f) the Eastern Alps, (g) the Dinarides and (h) the Adriatic zone.
Thin crust (< 40 km):

(a) *Carpathian arc*: the crust thickness varies from 30 km in the Internides to 40 km in the Externides. In the Western and Southern Carpathians, two local crustal depressions can be observed. The smaller Western Carpathian one reaches a thickness of 40–42 km and the greater Southern Carpathian one has a maximum thickness of 42.5 km.

(b) *Pannonian Basin*: a very thin crust (24–30 km).

(c) *East European Craton*: a very thick crust (45–60 km). Three crustal roots can be observed with the maximum crustal thicknesses of 50 km and 60 km.

(d) *West-Paleozoic European Platform (including the Bohemian Massif)*: the average crustal thickness varies from 27.5 km to 40 km.

(e) *Trans-European Suture Zone*: typical feature is a sharp drop of Moho from a depth of ∼37.5 km to ∼42.5 km. The drop is in the direction from SW to NE. The depth isolines have NW–SE direction, which correlates with the direction of this significant suture zone.

(f) *Eastern Alps*: thick crust (40 km).

(g) *Dinarides*: thick crust of about 40 km.

(h) *Adriatic zone*: the crustal thickness is ∼30 km.

The results indicate that the Moho depth variations depend mostly on the age of the latest thermal processes, which had been taking place in each of the tectonic units.

Acknowledgements. Special thanks are addressed to all people who participated in the acquisition of gravity data during a long observation history. This work was supported by the Slovak Grant Agency VEGA, grants No. 1/0141/15, 2/0042/15, and APVV grants No. APVV-16-0146, APVV-16-0482.

References

Alasonati Tašárová Z., Fullea J., Bielik M., Środa P., 2016: Lithospheric structure of Central Europe: Puzzle pieces from Pannonian Basin to Trans-European Suture Zone resolved by geophysical-petrological modelling. Tectonics, **35**, 1–32.

Aljinovič B., 1987: On certain characteristics of the Mohorovičič discontinuity in the region of Yugoslavia. Acta Geol. Yugosl. Akad. Znan. Umjet, **17**, 3–20.

Aric K., Gutdeutsch R., 1987: Geophysical aspects of the crustal structures of the Eastern Alps. In: Geodynamics of the Eastern Alps, Eds.: Fluegel H. W., Faupl P., Deuticke F., Verlag, 309–360.

Artemieva I. M., Thybo H., 2013: Moho discontinuity and crustal structure in Europe, Greenland, and the North Atlantic region. Tectonophysics, **609**, 97–153.

Behm M., Brückl E., Mitterbauer U., 2007: A New Seismic Model of the Eastern Alps its Relevance for Geodesy and Geodynamics. VGI Österrreichische Zeitschrift für Vermessung & Geoinformation, **2**, 121–133.

Beránek B., Zátopek A., 1981a: Earth's crust structure in Czechoslovakia and in Central Europe by methods of explosion seismology. In: Geophysical syntheses in Czechoslovakia. Ed.: Zátopek A., VEDA, 243–270.

Beránek B., Zátopek A., 1981b: Preliminary results of geophysical syntheses in Czechoslovakia and Central Europe based on explosion seismology until 1980. In: Geophysical Syntheses in Czechoslovakia, Veda, Bratislava, 469–497.

Brückl E., 2011: Lithospheric Structure and Tectonics of the Eastern Alps – Evidence from New Seismic Data. In: Tectonics, Ed.: Closson D., InTech, Available from: `http://www.intechopen.com/books/tectonics/lithospheric-structure-and-tectonics-of-the-eastern-alps-evidence-from-new-seismic-data`.

Brückl E., Behm M., Decker K., Grad M., Guterch A., Keller G. R., Thybo H., 2010: Crustal structure and active tectonics in the Eastern Alps. Tectonics, **29**, 1–17.

Brückl E., Bleibinhaus F., Gosar A., Grad M., Guterch A., Hrubcová P., Keller G. R., Majdański M., Šumanovac F. Tiira T., Yliniemi J., Hegedűs E., Thybo H., 2007: Crustal structure due to collisional and escape tectonics in the Eastern Alps region based on profiles Alp01 and Alp02 from the ALP 2002 seismic experiment. J. Geophys. Res., **112**, 1–25.

Bucha V., Blížkovský M. (Eds), 1994: Crustal structure of the Bohemian Massif and the West Carpathians. Springer-Verlag and Academia. Berlin, Heidelberger, New-York and Praha, 177–188.

Chekunov A. V., Ádám A. A., Blížkovský M., Bormann P., Guterch A., Dačev Ch., Kornea I., Kutas R. J., Magnickij V. A., Sollogub V. B., Chain V. E., Sollogub N. V., Starostenko V. J., 1988: Litosphere of Central and Eastern Europe: Geotraverses I, II, V. Naukova dumka, Kiev, 165. (in Russian).

Dérerová J., Zeyen H., Bielik M., Salman K., 2006: Application of integrated geophysical modeling for determination of the continental lithospheric thermal structure in the eastern Carpathians. Tectonics, **25**, TC3009.

Dimitrijevič M. D., 1995: The map of Moho surface and Bouguer gravity map. In: Geological Atlas of Serbia, 1:2000000, Ed.: Dimitrijevič M. D., Republ. Found Geological Investigations and RGF Geophysical Department.

Dragaševič T., 1987: The Mohorovičič discontinuity, structure and classification of the Earth crust in the eastern region of Yugoslavia. Acta Geod. Jugosl. Akad. Znam. Umjet, **17**, 39–45.

Gálfi J., Stegena L., 1960: Deep reflections and crustal structure in the Hungarian Basin. Ann. Univ. Sci. Bp. R. Eötvös nom., **3**, 41–47.

Grad M., Guterch A., Keller G. R., Janik T., Hegedűs E., Vozár J., Slaczka A., Tiira T., Yliniemi J., 2006: Lithospheric structure beneath trans-Carpathian transect from Precambrian platform to Pannonian Basin: CELEBRATION 2000 seismic profile CEL05. J. Geophys. Res., **111**, 1–23.

Grad M., Brückl E., Majdański M., Behm M., Guterch A., CELEBRATION 2000 and ALP 2002 Working Groups, 2009a: Crustal structure of the Eastern Alps and their foreland: seismic model beneath the CEL10/Alp04 profile and tectonic implications. Geophys. J. Int., **177**, 279–295.

Grad M., Tiira, T., ESC Working Group, 2009b: The Moho depth map of the European Plate. Geophys. J. Int., **176**, 279–292.

Grinč M., Zeyen H., Bielik M., Plašienka D., 2013: Lithospheric structure in Central Europe: Integrated geophysical modelling. J. Geodyn., **66**, 13–24.

Guterch A., Grad M., Materzok R., Perchuč E., Toporkiewicz S., 1986: Results of seismic crustal studies in Poland. Publ. Inst. Geophys. Pol. Acad. Sci., **17**, 192, 1–84. (in Polish with English summary).

Guterch A., Kowalski T. J., Materzok R., Toporkiewicz S., 1976: Seismic refraction study of the Earrth's crust in the Teisseyre-Tornquist line zone in Poland along the LT-2 profile. Publ. Inst. Geophys. Pol. Acad. Sci., A-2, **101**, 15–23.

Guterch A., Grad M., Materzok R., Pajchel J., Perchuč E., Toporkiewicz S., 1984: Deep structure of the Earth's crust in the contact zone of the Palaeozoic and Precambrian platforms and the Carpathian Mts in Poland. Acta Geophysica Polonica, **32**, 25–41.

Guterch A., Grad M., Materzok R., Toporkiewicz S., 1983: Structure of the earth's crust of the Permian Basin in Poland. Acta Geophysica Polonica **31**, 121–138.

Hauser F., Raileanu V., Fielitz W., Bala A., Prodehl C., Schulze A., 2001: VRANCEA99 – the crustal structure beneath the southeastern Carpathians and the Moesian Platform from a seismic tefraction profile in Romania. Tectonophysics, **430**, 233–256.

Hauser F., Raileanu V., Fielitz W., Dinu C., Landesa M., Bala A., Prodehl C., 2007: Seismic crustal structure between the Transylvanian Basin and the Black Sea. Tectonophysics, **430**, 1–25.

Horváth F., 1993: Towards a mechanical model for the formation of the Pannonian Basin. Tectonophysics, **226**, 333–357.

Horváth G., Bada F., Szafián P., Tari G.,Ádám A., Cloetingh S., 2006: Formation and deformation of the Pannonian Basin: Constraints from observational data. In: European Lithosphere Dynamics, Geol. Soc. Mem., **32**, Ed.: Gee D., Stephenson R., Geol. Soc., London. 191–206.

Hrubcová P., Środa P., 2015: Complex local Moho topography in the Western Carpathians: Indication of the ALCAPA and the European Plate contact. Tectonophysics, **638**, 63–81.

Hrubcová P., Środa P., CELEBRATION 2000 Working Group, 2008: Crustal structure at the easternmost termination of the Variscan belt based on CELEBRATION 2000 and ALP 2002 data. Tectonophysics, **460**, 55–75.

Hrubcová P., Środa P., Grad M., Geissler W. H., Guterch A., Vozár J., Hegedűs E., Sudetes Working Group, 2010: From the Variscan to the Alpine Orogeny: crustal structure of the Bohemian Massif and the Western Carpathians in the light of the SUDETES 2003 seismic data. Geophys. J. Int., **183**, 611–633.

Hrubcová P., Środa P., Špičák A., Guterch A., Grad M., Keller G. R., Brückl E., Thybo H., 2005: Crustal and uppermost mantle structure of the Bohemian Massif based on CELEBRATION 2000 data. J. Geophys. Res., **110**, 1–21.

Iľchenko T. V., Buharev V. P., 2001: Velocity model of the crust and upper mantle Korostensky Pluto (Ukrainian shield) and its geological interpretation (in profile DSS Shepetovka-Chernihiv). Geofizicheskij zhurnal, **23**, 72–82 (in Russian).

Janik T., Grad M., Guterch A., CELEBRATION 2000 Working Group, 2009: Seismic structure of the lithosphere between the East European Craton and the Carpathians from the net of CELEBRATION 2000 profiles in SE Poland. Geological Quarterly, **53**, 141–158.

Janik T., Grad M., Guterch A., Vozár J., Bielik M., Vozárová A., Hegedűs E., Kovács C. A., Kovács I., CELEBRATION 2000 Working Group, 2011: Crustal structure of the Western Carpathians and Pannonian Basin System: seismic models from CELEBRATION 2000 data and geological implication. J. Geodyn., **52**, 97–113.

Kaban M. K., Tesauro M., Cloetingh S., 2010: An integrated gravity model for Europe's crust and upper mantle, Earth Planet. Sci. Lett., **296**, 195–209.

Kharitonov O. M., Krasovskiy S. S., Kuprienko P. Ya., Kutas V. V., Sologub N. V., Drogitskaya G. M., Timoshenko V. I., Shlyahovskiy V. A., 1993: Lithospheric transect Vrancea-South-Ukrainian AES. Geofizicheskiy zhurnal, **15**, 23–31 (in Russian).

Kiss J., Gúthy T., Zilahi-Sebess L., 2015: Research of the Mohorovičič discontinuity in Hungary – methods, measurements and results. Magyar geofizika, **56**, 152–178 (in Hungarian, summary in English).

Knapp J. H., Knapp C. C., Raileanu V., Matenco L., Mocanu V., Dinu C., 2005: Crustal constraints on the origin of mantle seismicity in the Vrancea zone, Romania: the case for active continental lithospheric delamination. Tectonophysics, **410**, 311–323.

Lazarescu V., Cornea I., Radulescu F., Popescu M., 1983: Moho surface and recent crustal movements in Romania. Geodynamic connections. An. Inst. Geol. Geofiz., **63**, 83–91.

Lenkey L., Horváth F., Dövényi P., Szafián P., 1998: Geophysical features and structural conditions of the Pannonian Basin and its surroundings: a review. Rep. Geod. Warsaw Univ. Techn., **5**, 11–34.

Lenkey I., 1999: Geothermics of the Pannonian Basin and its bearing on the tectonics of Basin evolution. Phd. Thesis. Netherlands Research Scool of Sedimentary Geology publication No. 990112. Amsterdam: Vrije Universiteit Amsterdam, 1–215.

Malinowski M., CELEBRATION 2000 Working Group, 2003: Seismic crustal structure of the Alpine – Pannonian area revealed by the CELEBRATION 2000 experiment. Profiles CEL08 and CEL07. EGS–AGU–EGU Joint Assembly, Abstracts from the meeting held in Nice, France, 6–11 April 2003, abstract#2619.

Malinowski M., Guterch A., Narkiewicz M., Probulski J., Maksym A., Majdański M., Środa P., Czuba W., Gaczyński E., Grad M., Janik T., Jankowski L., Adamczyk A., 2013: Deep seismic reflection profile in Central Europe reveals complex pattern of Paleozoic and Alpine accretion at the East European Craton margin. Geophysical Research Letters, **40**, 1–6.

Malinowski M., Środa P., Grad M., Guterch A., CELEBRATION 2000 Working Group, 2009. Testing robust inversion strategies for three-dimensional Moho topography based on CELEBRATION 2000 data. Geophys. J. Int., **179**, 1093–1104.

Malinowski M., Żelaźniewicz A., Grad M., Guterch A., Janik T., CELEBRATION 2000 Working Group, 2005: Seismic and geological structure of the crust in the transition from Baltica to Palaeozoic Europe in SE Poland – CELEBRATION 2000 experiment, profile CEL02. Tectonophysics, **401** 55–77.

Martin M., Wenzel F., Calixto Working Group, 2006: High-resolution teleseismic body wave tomography beneath SE-Romania – II. Imaging of a slab detachment scenario. Geophys. J. Int., **164**, 579–595.

Mayerová M., Nakládalová Z., Ibrmajer I., Hermann H., 1985: Space distribution of the Moho surface in Czecho-Slovakia based on results of the DSS profile measurements and technical explosions. 8. Celoštátní konference geofyziků. Sekce S1-seizmická. Geofyzika, n.p. Brno, 44–53 (in Czech).

Mayerová, M., Novotný M., Fejfar, M., 1994: Deep seismic sounding in Czechoslovakia. In: Crustal structure of the Bohemian Massif and the West Carpathians. Eds.: Bucha V., Blížkovský M., Academia Press – Springer Verlag, 13–20.

Molinari I., Morelli A., 2011: EPcrust: a reference crustal model for the European Plate. Geophys. J. Int., **185**, 352–364.

Posgay K., Albu I., Mayerova M., Nakládalová Z., Ibrmajer I., Blížkovsky M., Aric K., Gutdeutsch R., 1991: Contour map of the Mohorovičič discontinuity beneath Central Europe. Geophys. Trans., **36**, 7–13.

Posgay K., Bodoky T., Hegedűs E., Kovácsvölgyi S., Lenkey L., Szafián P., Takács E., Tímár Z., Varga G., 1995: Asthenospheric structure beneath a Neogene Basin in SE Hungary. Tectonophysics, **252**, 467–484.

Posgay K., Takács E., Szalay I., Bodoky T., Hegedűs E., Kántor J. I., Timár Z., Varga G., Bérczi I., Szalay Á., Nagy Z., Pápa A., Hajnal Z., Reilkoff B., Mueller St., Ansorge J., De Iaco R., Asudeh I., 1996: International deep reflection survey along the Hungarian Geotraverse. Geophys. Trans., **40**, 1–44.

Šefara J., Bielik M., Bodnár J., Čížek P., Filo M., Gnojek I., Grecula P., Halmešová S., Husák Ľ., Janoštík M., Král M., Kubeš P., Kurkin M., Leško B., Mikuška J., Muška P., Obernauer D., Pospíšil L., Putiš M., Šutora A., Velich R., 1987: Structure-tectonic map of the Inner Western Carpathians for the prognoses of the ore deposits - geophysical interpretations. Explanation to the collection of the maps. Manuscript, 267 (in Slovak).

Sollogub V. B., 1986: Lithosphere of the Ukraine. Naukova dumka, Kiev, 172. (in Russian).

Sollogub V. B. (Ed.), 1988: Lithosphere of the Central and Eastern Europe: Geotraverses IV, VI, VIII. Naukova dumka, Kiev, 172.

Sollogub V. B., Prosen D., Dachev C., Petkov I., Vetchev T., Andonova E., Mihailov S., Mituch E., Posgay K., Militzer H., Knothe C., Uchman I., Constantinescu I., Cornea I., Subbotin S. I., Chekunov A. V., Garkalenko I. A., Khain V. E., Slavin V. I., Beranek B., Weiss J., Hrdlička A., Dudek A., Zounkova M., Suk M., Feifar M., Milovanović B., Roksandić M., 1973: Crustal structure of Central and Southeastern Europe by data of explosion seismology. Tectonophysics, **20**, 1–33.

Środa P., Czuba W., Grad M., Guterch A., Tokarski A. K., Janik T., Rauch M., Keller G. R., Hegedűs E., Vozár J., Celebration 2000 Working Group, 2006: Crustal and upper mantle structure of the Western Carpathians from CELEBRATION 2000 profiles CEL01 and CEL04: seismic models and geological implications. Geophys. J. Int., **167**, 737–760.

Starostenko V., Janik T., Kolomiyets K., Czuba W., Środa P., Grad M., Kovacs I., Stephenson R., Lysynchuk D., Thybo H., Artemieva I., Omelchenko V., Gintov O., Kutas R., Gryn D., Guterch A., Hegedűs E., Komminaho K., Legostaeva O., Tiira T., Tolkunov A., 2013: Seismic velocity model of the crust and upper mantle along profile PANCAKE across the Carpathians between the Pannonian Basin and the East European Craton. Tectonophysics, **608**, 1049–1072.

Szafián P., Horváth F., Cloetingh S., 1997: Gravity constrains on the crustal structure and slab evolution along a trans-Carpathian transect. Tectonophysics, **272**, 233–247.

Szafián P., Horváth F., 2006: Crustal structure in the Carpatho-Pannonian region: insights from three-dimensional gravity modelling and their geodynamic significance. Int. J. Earth Sci. (Geol. Rundsch.), **95**, 50–67.

Szénás Gy. (Ed), 1972: The crustal structure of Central and Southeastern Europe based on the results of explosion seismology. Spec. Edit. Geophys. Transact., 1–172.

Tesauro M., Kaban M. K., Cloetingh S., 2008: EuCRUST-07: A new reference model for the European crust. Geophys. Res. Lett., **35**, L05313.

Zeyen H., Dérerová J., Bielik M., 2002: Determination of the continental lithosphere thermal structure in the Western Carpathians: integrated modelling of surface heat flow, gravity anomalies and topography. Physics of the Earth and Planetary Interiors, **134**, 89–104.

Ziegler P. A., Dezes P., 2006: Crustal evolution of Western and Central Europe. In: European Lithosphere Dynamics. Eds.: Gee D., Stephenson R., Geol. Soc. London Sp. Publ., **32**, 43–56.